



**HAL**  
open science

# Continuum damage analysis of delamination in composite laminates using a stress-based layerwise plate model

Paul Bouteiller, Jeremy Bleyer, Karam Sab

► **To cite this version:**

Paul Bouteiller, Jeremy Bleyer, Karam Sab. Continuum damage analysis of delamination in composite laminates using a stress-based layerwise plate model. *International Journal of Solids and Structures*, 2022, pp.111611. 10.1016/j.ijsolstr.2022.111611 . hal-03639729

**HAL Id: hal-03639729**

**<https://enpc.hal.science/hal-03639729>**

Submitted on 13 Apr 2022

**HAL** is a multi-disciplinary open access archive for the deposit and dissemination of scientific research documents, whether they are published or not. The documents may come from teaching and research institutions in France or abroad, or from public or private research centers.

L'archive ouverte pluridisciplinaire **HAL**, est destinée au dépôt et à la diffusion de documents scientifiques de niveau recherche, publiés ou non, émanant des établissements d'enseignement et de recherche français ou étrangers, des laboratoires publics ou privés.

# Continuum damage analysis of delamination in composite laminates using a stress-based layerwise plate model

Paul Bouteiller<sup>a</sup>, Jeremy Bleyer<sup>a,\*</sup>, Karam Sab<sup>a</sup>

<sup>a</sup>Laboratoire Navier, ENPC, Univ Gustave Eiffel, CNRS,  
Cité Descartes, 6-8 av Blaise Pascal, 77455 Champs-sur-Marne, FRANCE

---

## Abstract

This contribution addresses the modelling of delamination in a stress-based layerwise plate model. Such models benefit from a good representation of the local 3D stress field, especially inter-laminar stresses which are natural generalized stress unknowns arising in their derivation. We extend their construction to situations involving onset and propagation of interfacial delamination. We propose a variational formulation relying on a continuous damage description of the opening and sliding interfacial degradation processes using two damage variables. A mixed-mode delamination propagation criterion can be obtained through proper coupling between both variables. Finally, the model predictions are validated against classical delamination tests in pure and mixed modes.

*Keywords:* generalized continuum, stress-based model, multilayered plates, delamination, damage model, variational approach

---

## 1. Introduction

Laminated composites are commonly encountered in industrial applications where the problem of mass is critical. Growing demand to obtain lightweight designs with higher damage tolerance implies a comprehensive understanding of the mechanisms involved during the failure processes. The strong anisotropy of the constituent plies and the stacking sequence induces important inter-laminar stresses, leading to the onset and propagation of delamination. Delamination is one of the most critical mechanisms affecting the structural integrity in industrial applications. Moreover, it is most often imperceptible to an operator's eye inspection [1] and must therefore be modelled accurately.

Alongside the J-integral and the virtual crack closure technique[2–4], the most common way of modelling delamination in composite laminates is to resort to a full 3D modelling of the multilayered plate in conjunction with interface elements which employ a Cohesive Zone Model (CZM) of the interfacial behaviour.

---

\*Correspondence to: J. Bleyer, Laboratoire Navier, 6-8 av Blaise Pascal, Cité Descartes, 77455 Champs-sur-Marne, France, Tel : +33 (0)1 64 15 37 43

Email addresses: paul.bouteiller@enpc.fr (Paul Bouteiller), jeremy.bleyer@enpc.fr (Jeremy Bleyer), karam.sab@enpc.fr (Karam Sab)

URL: <https://sites.google.com/site/bleyerjeremy/> (Jeremy Bleyer)

Interface CZM elements can efficiently predict both the onset and propagation of delamination since the fracture plane is known in advance. Besides, upon proper coupling between both opening (mode I) and shearing (mode II) fracture modes, mixed mode propagation criterion can also be considered. However, the use of 3D solid elements and interface CZM poses some difficulties in terms of robustness and computational costs. Indeed, owing to the high slenderness of composite plates, the retained mesh size must be quite small to avoid 3D elements being too elongated which would be detrimental to the solution accuracy and system conditioning. Convergence difficulties of the underlying nonlinear solver are also widely reported in the literature [5–8] which are heavily influenced by the shape of the cohesive law, the choice of the tangent operator, the numerical quadrature, the mesh size, the critical stress, etc. Finally, the use of intrinsic CZM also introduces a somewhat artificial elastic stiffness of the interface the value of which is not always easy to choose properly. In addition to softening the laminate structural stiffness, it plays also an important role in the convergence behaviour of the numerical iterative process.

An alternative to a 3D CZM modelling is to resort to two-dimensional layerwise plate models, such as Reddy’s [9, 10] or those based on the Carrera Unified Formulation (CUF) [11, 12] enable to obtain an enhanced description kinematics through the thickness. Recently, only a few works have considered delamination in layerwise models such as 1D CUF models [13], 2D CUF models with impact [14], mode II propagation with a refined zig-zag theory [15], layerwise beam models in mixed-mode propagation [16] or a Rayleigh-Ritz formulation for buckling-induced delamination [17].

In such displacement-based approaches, interlaminar stresses are only obtained as a result from the thickness displacement expansion and may not be evaluated accurately enough in general. Although including high-order kinematics in each layer may improve the stress predictions, another possibility is to resort to stress-based layerwise models, in which stresses (and in particular, interlaminar stresses) appear as naturally emerging quantities in such models. For instance, [18] first proposed a polynomial expansion of the stress field in each layer. Simplified models have been later proposed based on this work such as the M4-2n+1 model [19, 20] or the more-refined M4-5n model [19, 21–23], now renamed LS1 model<sup>1</sup> to fit the CUF nomenclature, or the most recent SCLS1 model [24–26]. In particular, such models have been shown to properly capture free-edge effects and yield an accurate prediction of stress singularities near delaminated areas [20, 27, 28]. A first proposal to model the propagation of delamination in a 1D setting using the Virtual Crack Closure Technique (VCCT) has been proposed in [29] using the LS1 model whereas [30] considered the case of elastoplastic interfaces. As a result, there exist no contribution on a stress-based layerwise 2D plate models capable of handling the onset and propagation of delamination in multiple interfaces and mixed-mode loading. The present work therefore aims at bridging this gap. To do so, we consider the

---

<sup>1</sup>Layerwise Stress model of degree 1 (polynomial degree of the membrane stresses)

stress-based layerwise model and formulate a continuum damage model in order to describe the progressive evolution of delamination in both mode I and mode II.

The paper is organized as follows: Section 2 is dedicated to a brief reminder of the theoretical formulation of the LS1 model. We also discuss how delaminated interfaces affect the laminate generalized stiffness matrix. Section 3 introduces a new model which we call Lumped-LS1 model and which approximates the corresponding out-of-plane and shear complementary energies to obtain a much simpler generalized model with a diagonal structure. This model is then used for the formulation of a generalized continuum damage model that is thermodynamically consistent and which benefits from a variational formulation, as detailed in section 4. Section 5 then discusses the expression of the damaged-dependent elastic strain energy whereas section 6 details some key elements of the numerical implementation. Finally, section 7 presents the validation of the proposed approach on classical pure and mixed-mode delamination tests and illustrates its efficiency on a multi-interface problem.

## 2. The stress-based layerwise LS1 model

### 2.1. Reminder of the LS1 model derivation

We here briefly remind the main characteristics of the considered LS1 layerwise model. For the sake of concision, the reader can refer to Appendix A for additional details regarding notations and derivation of the model.

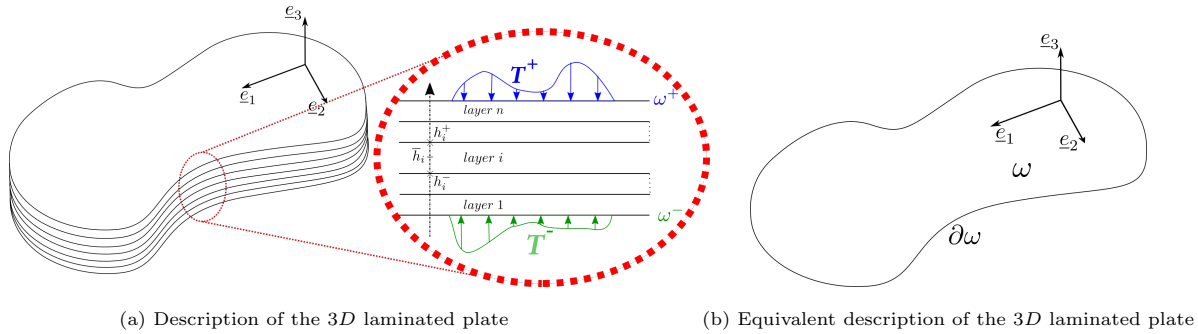


Figure 1: Description of the laminated plate

In the following, we consider a 3D plate domain  $\Omega$  consisting of  $n$  layers of thickness  $e^i$  of reference middle plane  $\omega$  in the  $(x_1, x_2)$  in-plane directions,  $x_3$  being the out-of-plane direction. In each layer  $i$ ,  $h_i^-$ ,  $h_i^+$  and  $\bar{h}_i$  are, respectively, the bottom, top and mid-plane  $x_3$ -coordinate of the layer. Each ply is initially assumed to be perfectly bonded to each other and is made of an orthotropic elastic material of compliance fourth-order tensor  $S_{mnpq}^i$ . The pair  $j, j + 1$  refers to the interface between layer  $j$  and  $j + 1$ . By extension, the pair  $0, 1$  corresponds to the plate lower face  $\omega^-$  and  $n, n + 1$  to the upper face  $\omega^+$ .

The LS1 model is obtained from a specific Ansatz on the local 3D stress field  $\boldsymbol{\sigma}^{3D}(\boldsymbol{x})$  along the  $x_3$ -direction as a function of some generalized stresses vector  $\boldsymbol{\Sigma}(x_1, x_2)$ . More precisely, the main hypothesis is that the membrane stresses  $\sigma_{\alpha\beta}^{i,3D}$  in layer  $i$  are assumed to be an affine function of  $x_3$ . In order to satisfy the local equilibrium equation without body forces, the shear stresses  $\sigma_{\alpha 3}^{i,3D}$  must be quadratic in  $x_3$ , whereas the out-of-plane stress  $\sigma_{33}^{i,3D}$  must be cubic in  $x_3$ , see (A.1)-(A.2)-(A.3). The involved generalized stresses  $\boldsymbol{\Sigma}$  in this polynomial expansion have simple physical meanings since they consist of:

- $\boldsymbol{N}^i$ : the in-plane stress resultant tensor in layer  $i$ ,
- $\boldsymbol{M}^i$ : the bending moment resultant tensor in layer  $i$ ,
- $\boldsymbol{Q}^i$ : the resultant shear forces vector in layer  $i$ ,
- $\tau^{i,i+1}$ : the inter-laminar shear stress at the interface between the layer  $i$  and  $i+1$ ,
- $\nu^{i,i+1}$  the out-of plane stress at the interface between the layer  $i$  and  $i+1$ .

The last two quantities are related to the local 3D stress field at the corresponding interface as follows:

$$\sigma_{\alpha 3}^{i,3D}(x_1, x_2, h_i^+) = \tau_{\alpha}^{i,i+1}(x_1, x_2) \quad (1)$$

$$\sigma_{33}^{i,3D}(x_1, x_2, h_i^+) = \nu^{i,i+1}(x_1, x_2) \quad (2)$$

and therefore provide direct access to quantities of interest (inter-laminar stresses) for the study of delamination.

The local 3D equilibrium equations translate into  $5n$  equilibrium equations linking our generalized stresses:

$$N_{\alpha\beta,\beta}^i + \tau_{\alpha}^{i,i+1} - \tau_{\alpha}^{i-1,i} = 0 \quad (3a)$$

$$M_{\alpha\beta,\beta}^i - Q_{\alpha}^i + \frac{e^i}{2}(\tau_{\alpha}^{i,i+1} + \tau_{\alpha}^{i-1,i}) = 0 \quad (3b)$$

$$Q_{\alpha,\alpha}^i + \nu^{i,i+1} - \nu^{i-1,i} = 0 \quad (3c)$$

The dual kinematic quantities associated with each equilibrium equation (3a)–(3c) represent the generalized displacements  $\boldsymbol{U}$  of the LS1 model which can be interpreted in terms of specific weighted averages of the 3D local displacement field (see [11], [21], for more details). In a nutshell,  $\boldsymbol{U}$  is of size  $5n$  and consists of layerwise in-plane displacements  $U_{\alpha}^i$  (associated with (3a)), in-plane rotations  $\Phi_{\alpha}^i$  (associated with (3b)) and out-of-plane displacement  $U_3^i$  (associated with (3c)). As a result, the proposed model can be seen as a collection of individual layers, possessing a Reissner-Mindlin kinematics and in interaction with each other.

Upon writing the weak form associated with the above strong equilibrium equations, the corresponding generalized strains  $\boldsymbol{E}$  appearing in duality with the generalized stresses  $\boldsymbol{\Sigma}$  are obtained. Their expression in terms of  $\boldsymbol{U}$  are given in (A.4).

Finally, the LS model's generalized elastic constitutive law is obtained through the minimum complementary energy principle. Upon integrating the local elastic energy through the thickness and after some simplifying approximations which have been detailed in [24, 31], one obtains the corresponding generalized complementary elastic energy density:

$$\Psi^*(\boldsymbol{\Sigma}) = \frac{1}{2} \boldsymbol{\Sigma} \mathbb{S} \boldsymbol{\Sigma} \quad (4)$$

which enables to derive the generalized elastic constitutive law as follows:

$$\mathbf{E}^{\text{el}} = \frac{\partial \Psi^*}{\partial \boldsymbol{\Sigma}} = \mathbb{S} \boldsymbol{\Sigma} \quad (5)$$

where  $\mathbb{S}$  designates the generalized compliance matrix and  $\mathbf{E}^{\text{el}}$  is the generalized elastic strain. Note that, in presence of surface loading on the top or bottom surfaces  $\omega^\pm$ , the elastic strain is given by  $\mathbf{E}^{\text{el}} = \mathbf{E} - \mathbf{E}^0$  where  $\mathbf{E}^0$  can be interpreted as a loading-induced pre-strain. Equivalently, the above elastic law can be written as  $\boldsymbol{\Sigma} = \mathbb{C} \mathbf{E}^{\text{el}}$  where  $\mathbb{C} = \mathbb{S}^{-1}$  denotes the laminate generalized stiffness matrix at a given point  $\mathbf{x} = (x_1, x_2) \in \omega$ .

An important aspect for the following discussion is that the generalized compliance  $\mathbb{S}$  enjoys a block-diagonal structure (we refer to Appendix A.4 for the detailed expressions). In particular, the membrane-bending compliance  $\mathbb{S}^K$  associated with  $(\mathbf{N}^i, \mathbf{M}^i)$ , the peeling compliance  $\mathbb{S}^\nu$  associated with the  $\nu^{i,i+1}$  and the shear compliance  $\mathbb{S}^Q$  associated with  $(\mathbf{Q}^i, \boldsymbol{\tau}^{i,i+1})$  are decoupled from each other. In addition,  $\mathbb{S}^K$  possesses a further block-structure per layer so that the membrane/bending compliance of each layer is decoupled from one another. However, this is not the case for both  $\mathbb{S}^\nu$  and  $\mathbb{S}^Q$ . Indeed, the former enjoys a tridiagonal structure whereas the latter is pentadiagonal. The corresponding generalized stiffnesses  $\mathbb{C}^\nu = (\mathbb{S}^\nu)^{-1}$  and  $\mathbb{C}^Q = (\mathbb{S}^Q)^{-1}$  are therefore full matrices in general. This aspect is a key feature of such stress-based layerwise models and introduces an additional complexity when attempting at building a damage model for interfacial delamination.

## 2.2. Generalized stiffness in presence of delaminated interfaces

We now discuss how the LS1 model generalized stiffness  $\mathbb{C}$  is modified in presence of delaminated interfaces. Let us consider a given interface  $m, m+1$  in the stacking sequence which we now assume to be fully delaminated at a given point  $\mathbf{x} \in \omega$ . In this case, the inter-laminar stresses should vanish i.e.  $\nu^{m,m+1} = 0$  and  $\tau_\alpha^{m,m+1} = 0$ . We formally note these conditions as  $\mathbf{T}^\top \boldsymbol{\Sigma} = 0$  where  $\mathbf{T}$  is a rectangular matrix with 0/1 entries. This generic notation can therefore generalize the previous conditions to multiple delaminated interfaces. When deriving the elastic strain  $\mathbf{E}^{\text{el}}$  from the generalized elastic complementary energy  $\Psi^*(\boldsymbol{\Sigma})$  in presence of such internal constraints, an associated Lagrange multiplier  $\boldsymbol{\mu}$  appears such that:

$$\mathbf{E}^{\text{el}} = \frac{\partial \Psi^*}{\partial \boldsymbol{\Sigma}} + \frac{\partial (\mathbf{T}^\top \boldsymbol{\Sigma})}{\partial \boldsymbol{\Sigma}} \boldsymbol{\mu} = \mathbb{S} \boldsymbol{\Sigma} + \mathbf{T} \boldsymbol{\mu} \quad (6)$$

Inverting the above equation and inserting into the stress-free constraint  $\mathbf{T}^\top \boldsymbol{\Sigma} = 0$ , we obtain:

$$\mathbf{T}^\top \boldsymbol{\Sigma} = \mathbf{T}^\top \mathbb{C}(\mathbf{E}^{\text{el}} - \mathbf{T}\boldsymbol{\mu}) = 0 \quad (7)$$

$$\boldsymbol{\mu} = \left(\mathbf{T}^\top \mathbb{C} \mathbf{T}\right)^{-1} \mathbf{T}^\top \mathbb{C} \mathbf{E}^{\text{el}} \quad (8)$$

$$\boldsymbol{\Sigma} = \mathbb{C}^{\text{d}} \mathbf{E}^{\text{el}} \quad (9)$$

where the ‘‘delaminated’’ generalized stiffness matrix is given by:

$$\mathbb{C}^{\text{d}} = \mathbb{C} - \mathbb{C} \mathbf{T} \left(\mathbf{T}^\top \mathbb{C} \mathbf{T}\right)^{-1} \mathbf{T}^\top \mathbb{C} \quad (10)$$

Thanks to the block structure of  $\mathbb{S}$  and thus of  $\mathbb{C}$ , (9) is divided into two sub-operations: namely the computation of the delaminated out-of-plane stiffness  $\mathbb{C}_\nu^{\text{d}}$  and the delaminated shear-stiffness  $\mathbb{C}_Q^{\text{d}}$  (see Appendix A.5 for details). For instance, the out-of-plane stiffness matrix of a 5 plies, 4 interfaces, laminated composite, divided in 2 parts by the delamination of the interface between plies 2 and 3 reads:

$$\mathbb{C}_\nu^{2,\text{d}} = \begin{pmatrix} c_{11}^\nu - \frac{(c_{12}^\nu)^2}{c_{22}^\nu} & 0 & c_{13}^\nu - \frac{c_{12}^\nu c_{23}^\nu}{c_{22}^\nu} & c_{14}^\nu - \frac{c_{12}^\nu c_{24}^\nu}{c_{22}^\nu} \\ & 0 & 0 & 0 \\ & & c_{33}^\nu - \frac{(c_{23}^\nu)^2}{c_{22}^\nu} & c_{34}^\nu - \frac{c_{23}^\nu c_{24}^\nu}{c_{22}^\nu} \\ \text{SYM.} & & & c_{44}^\nu - \frac{(c_{24}^\nu)^2}{c_{22}^\nu} \end{pmatrix} \quad (11)$$

where  $c_{ij}^\nu$  are the entries of the initial out-of-plane stiffness  $\mathbb{C}^\nu$ . Interestingly, due to the stress-based nature of the LS1 model, the presence of a delaminated interface does not split the out-of-plane stiffness into two independent blocks as off-diagonal coupling terms still exist.

### 3. A new Lumped-LS1 model

One difficulty when extending such stress-based layerwise plate models arises from the existence of couplings between generalized stresses in the generalized compliance matrix, yielding, in general a full generalized stiffness matrix when inverting the latter as discussed before. Such formulations also make it difficult to use local 3D nonlinear constitutive behaviours whereas the derivation of nonlinear constitutive equations based on generalized stresses is not an easy task either. For all these reasons, simpler formulations of the stress-based model would be beneficial to its extension towards nonlinear behaviours. This is the purpose of the present section.

### 3.1. Approximate out-of-plane behaviour

When evaluating the contribution of layer  $j$  to the out-of-plane elastic energy density in the original LS1 model, one obtains:

$$\begin{aligned}\psi_\nu^j &= \frac{1}{2}e^j S_{3333}^j \left( \frac{13}{35}(\nu^{j-1,j})^2 + \frac{13}{35}(\nu^{j,j+1})^2 + \frac{18}{70}\nu^{j-1,j}\nu^{j,j+1} \right) \\ &= \frac{1}{2}e^j S_{3333}^j \left\{ \nu^{j-1,j} \quad \nu^{j,j+1} \right\} \begin{pmatrix} \frac{13}{35} & \frac{9}{70} \\ \frac{9}{70} & \frac{13}{35} \end{pmatrix} \begin{Bmatrix} \nu^{j-1,j} \\ \nu^{j,j+1} \end{Bmatrix}\end{aligned}\quad (12)$$

which induces coupling between adjacent layers due to the off-diagonal term. To avoid such a coupling, we therefore propose to replace the above computation with the following approximation:

$$\begin{aligned}\psi_\nu^j &\approx \frac{1}{2}e^j S_{3333}^j \left( \frac{1}{2}(\nu^{j-1,j})^2 + \frac{1}{2}(\nu^{j,j+1})^2 \right) \\ &= \frac{1}{2}e^j S_{3333}^j \left\{ \nu^{j-1,j} \quad \nu^{j,j+1} \right\} \begin{pmatrix} \frac{1}{2} & 0 \\ 0 & \frac{1}{2} \end{pmatrix} \begin{Bmatrix} \nu^{j-1,j} \\ \nu^{j,j+1} \end{Bmatrix}\end{aligned}\quad (13)$$

which results in an expression which does not induce such couplings. The above approximate expression can be seen as a *mass-lumping* procedure as commonly done in structural dynamics.

### 3.2. Approximate shear behaviour

In the original formulation of the LS1 model, the out-of-plane shear stress  $\sigma_{\alpha 3}^i$  in layer  $i$  is expressed as a quadratic polynomial in  $x_3$  parametrized by the interfacial shear stresses  $\tau_\alpha^{i-1,i}$ ,  $\tau_\alpha^{i,i+1}$  and the resultant shear force  $Q_\alpha^i$ . In order to derive an approximation similar to the out-of-plane behaviour, we reformulate the out-of-plane shear stress as a function of the mid-layer shear stress  $\bar{\tau}_\alpha^i = \sigma_{\alpha 3}^i(x_3 = \bar{h}_i)$  instead of the shear force  $Q_\alpha^i$ :

$$\sigma_{\alpha 3}^i(x_3) = y(2y-1)\tau_\alpha^{i-1,i} + (1-4y^2)\bar{\tau}_\alpha^i + y(2y+1)\tau_\alpha^{i,i+1}\quad (14)$$

where  $y = (x_3 - \bar{h}_i)/e^i$ .

The contribution of the out-of-plane shear of layer  $i$  to the elastic energy density reads:

$$\begin{aligned}\psi_\tau^i &= \frac{1}{2} \int_{h_i^-}^{h_i^+} 4S_{\alpha 3 \beta 3}^i \sigma_{\alpha 3} \sigma_{\beta 3} dx_3 \\ &= \frac{1}{2} 4e^i S_{\alpha 3 \beta 3}^i \frac{1}{30} (\boldsymbol{\tau}_\alpha^i)^\top \begin{pmatrix} 4 & 2 & -1 \\ 2 & 16 & 2 \\ -1 & 2 & 4 \end{pmatrix} \boldsymbol{\tau}_\beta^i\end{aligned}\quad (15)$$

where  $\boldsymbol{\tau}_\alpha^i = \left\{ \tau_\alpha^{i-1,i} \quad \bar{\tau}_\alpha^i \quad \tau_\alpha^{i,i+1} \right\}^\top$ . Again, off-diagonal terms induce a coupling between adjacent layers. Similarly to the out-of-plane term, we therefore propose to "lump" the corresponding matrix at the layer

bottom, mid and top planes as follows:

$$\psi_\tau^i \approx \frac{1}{2} 4e^i S_{\alpha 3 \beta 3}^i \frac{1}{6} (\boldsymbol{\tau}_\alpha^i)^T \begin{pmatrix} 1 & 0 & 0 \\ 0 & 4 & 0 \\ 0 & 0 & 1 \end{pmatrix} \boldsymbol{\tau}_\beta^i \quad (16)$$

Note that such a lumping procedure is equivalent to using a Simpson quadrature rule to evaluate the integral in (15) approximately.

### 3.3. Generalized behaviour

As a result of the above lumping approximation, the corresponding generalized behaviour now possesses a diagonal block structure, in particular regarding the out-of-plane and shear parts of the behaviour. The corresponding out-of-plane strain energy reads:

$$\frac{1}{2} \mathbf{E}_\nu^T \mathbf{C}_\nu \mathbf{E}_\nu = \frac{1}{2} \sum_{i=1}^{n-1} c_\nu^{i,i+1} (\varepsilon_\nu^{i,i+1})^2 \quad (17)$$

where  $\varepsilon_\nu^{i,i+1}$  is the corresponding out-of-plane generalized strain and:

$$c_\nu^{i,i+1} = \frac{2}{e^i S_{3333}^i + e^{i+1} S_{3333}^{i+1}} \quad (18)$$

The shear strain energy reads:

$$\frac{1}{2} \mathbf{E}_\tau^T \mathbf{C}_\tau \mathbf{E}_\tau = \frac{1}{2} \sum_{i=1}^{n-1} c_{\tau,\alpha\beta}^{i,i+1} D_\alpha^{i,i+1} D_\beta^{i,i+1} \quad (19)$$

$$+ \frac{1}{2} \sum_{i=1}^n \bar{c}_{\tau,\alpha\beta}^i \bar{D}_\alpha^i \bar{D}_\beta^i \quad (20)$$

where:

$$[c_{\tau,\alpha\beta}^{i,i+1}] = 6 \left( e^i [4S_{\alpha 3 \beta 3}^i] + e^{i+1} [4S_{\alpha 3 \beta 3}^{i+1}] \right)^{-1} \quad (21)$$

$$[\bar{c}_{\tau,\alpha\beta}^i] = \frac{3}{2e^i} [4S_{\alpha 3 \beta 3}^i]^{-1} \quad (22)$$

### 3.4. Free-edge effect

The consistent LS1 model presented in Section 2 has proven its remarkable accuracy to compute singular interface stresses in the vicinity of the free edges in laminated composites [32]. The lumped LS1 model simplifies the evaluation of the shear and out-of-plane when computing the complementary energy. This approximation must however be assessed in a critical configuration in which shear and out-of-plane stresses exhibit strong variations. We therefore consider a  $(0, 90)_s$  plate subject to uniaxial tension in the  $0^\circ$  direction. The Poisson's ratio effect induces a singular shear stress at the interface between the  $0$  and  $90$  plies. The Lumped-LS1 and LS1 models are compared with a highly refined 3D finite element reference. The

Material parameters		Geometric parameters
$E_L = 130 \text{ GPa}$	$E_T = E_N = 7.7 \text{ GPa}$	$e = 0.14 \text{ mm}$ $b = 8e$
$G_{LT} = G_{LN} = 4.8 \text{ GPa}$	$\nu_{LT} = \nu_{TN} = \nu_{LN} = 0.33$	

Table 1: Material and geometric properties of the free-edge effect analysis

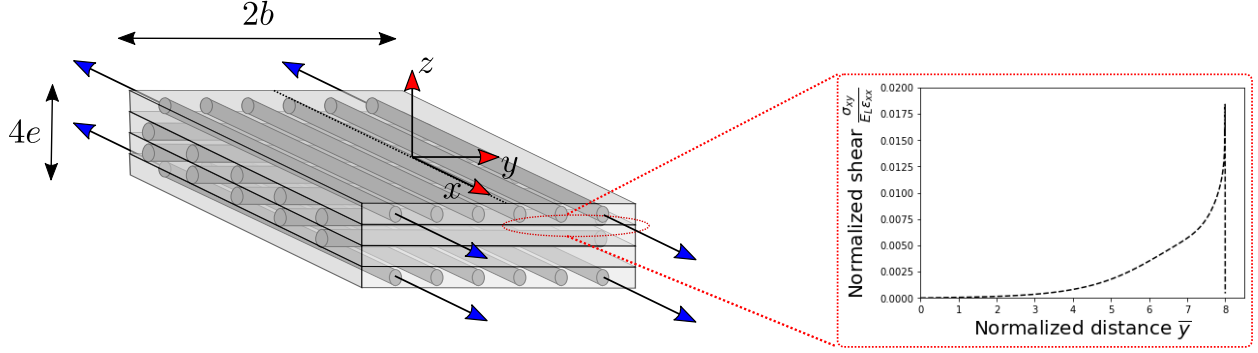


Figure 2: Uniaxial extension of a  $(0, 90)_s$  laminate

geometric and material parameters of a T700GC/M21 type carbon fiber [33] are reported in Table 1 (see also Figure 2).

The normalized inter-laminar shear stress  $\frac{\sigma_{xy}}{E_L \varepsilon_{xx}}$ , as a function of the normalized distance  $\bar{y} = y/e$  is shown in Figure 3. The overall agreement is very good up to very small distances to the edge. At edge

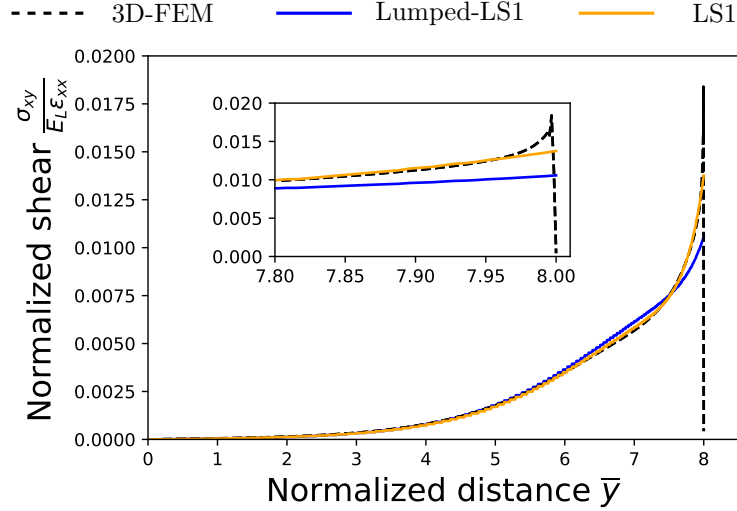


Figure 3: Normalized shear at the interface between the  $0^\circ$  and  $90^\circ$  plies.

distances less than one fifth of the ply thickness, the predictions of the highly refined 3D model and our model begin to differ. Obviously, the LS1 consistent model is much more accurate in capturing strong singularities,

however, the difference with the lumped model is only significant at such small scales that considering the material as a homogeneous anisotropic continuum is no longer relevant. Whether the difference observed in the peak stress near the edge is important or not will be assessed in the following sections when investigating initiation and propagation of delamination.

#### 4. Variational approach of continuum damage

We now proceed to the modeling of progressive delamination in our layerwise plate model, in which each interface is susceptible to experience delamination due to excessive inter-laminar normal or shear-stress. In this work, we make the modeling choice of proposing an ad hoc generalized damage model to account for such a phenomenon instead of relying on cohesive interface behaviours between the plies which may have required the introduction of an artificial interface stiffness. In the following, we rely on a thermodynamic formulation based on the framework of generalized standard materials (GSM) [34, 35].

For this purpose, we consider a vector-valued internal variable  $\mathbf{d}$  representing the inter-laminar degradation of the layered structure. It consists of two scalar damage variables  $d_\nu^{m,m+1}, d_\tau^{m,m+1}$  for each interface which will enable us to model the mixed-mode interaction between mode I and mode II delamination. The generalized stored elastic energy is therefore assumed to be coupled with damage  $\Psi(\mathbf{E}, \mathbf{d})$  as discussed later in section 5. In addition, we also consider a dissipation pseudo-potential  $\Phi$  of the damage rate  $\dot{\mathbf{d}}$ , possibly parametrized by the value of the damage variable  $\mathbf{d}$ . We assume that each interface contributes similarly and independently to the dissipation potential so that:

$$\Phi(\dot{\mathbf{d}}; \mathbf{d}) = \sum_{m=1}^{n-1} \phi(\dot{\boldsymbol{\alpha}}^m; \boldsymbol{\alpha}^m) + I_{\mathbb{R}^+}(\dot{\mathbf{d}}) \quad (23)$$

where  $\boldsymbol{\alpha}^m = (d_\nu^{m,m+1}, d_\tau^{m,m+1})$  for interface  $m$ ,  $\phi(\dot{\boldsymbol{\alpha}}^m; \boldsymbol{\alpha}^m)$  is the interface dissipation pseudo-potential which we assume to be a convex positively homogeneous function of  $\dot{\boldsymbol{\alpha}}^m$  (rate-independent behaviour).

Within the GSM framework, we readily obtain the following damage evolution laws:

$$\mathbf{Y} = -\frac{\partial \Psi}{\partial \mathbf{d}} \quad (24)$$

$$\mathbf{Y} \in \partial_{\dot{\mathbf{d}}} \Phi(\dot{\mathbf{d}}; \mathbf{d}) \quad (25)$$

where  $\mathbf{Y}$  is the thermodynamic force associated with  $\mathbf{d}$  and  $\partial_{\dot{\mathbf{d}}} \Phi$  denotes the pseudo-differential of  $\Phi$ .

Accounting for (23), the evolution equation can be rewritten for each interface  $m$  as:

$$\mathbf{Y}^m = -\frac{\partial \Psi}{\partial \boldsymbol{\alpha}^m} \leq \frac{\partial \phi}{\partial \dot{\boldsymbol{\alpha}}^m} \quad (26)$$

if  $\phi$  is differentiable with respect to  $\dot{\boldsymbol{\alpha}}^m$ . This defines the corresponding damage criterion in the  $\mathbf{Y}$ -space.

#### 4.1. Dissipation potential and delamination propagation criterion

We now specify the choices made for the damage dissipation potential. We essentially aim at formulating a mixed-mode propagation criterion accounting for the interaction between mode I and mode II energy release rates and their associated fracture energies  $G_{\text{Ic}}, G_{\text{IIc}}$ .

For this purpose, many mixed-mode interaction criteria have been proposed in the literature such as the power-law criterion ([36–38]):

$$\left(\frac{G_{\text{I}}}{G_{\text{Ic}}}\right)^{\alpha} + \left(\frac{G_{\text{II}}}{G_{\text{IIc}}}\right)^{\gamma} \leq 1 \quad (27)$$

for which the particular case  $\alpha = 1, \gamma = 1$  yields the linear criterion [39–42]. One can also mention the Benzeggagh-Kenane criterion [43]. A complete presentation of delamination criterion can be found for instance in [44]. In the following, we will focus on the power law interpolation (27) with  $\alpha = \gamma$ :

$$\left(\frac{G_{\text{I}}}{G_{\text{Ic}}}\right)^{\gamma} + \left(\frac{G_{\text{II}}}{G_{\text{IIc}}}\right)^{\gamma} \leq 1 \quad (28)$$

Dropping the interface superscript  $m$  for simplicity, let us introduce the following function:

$$\varphi(\boldsymbol{\alpha}) = \varphi(d_{\nu}, d_{\tau}) = ((G_{\text{Ic}}w_{\nu}(d_{\nu}))^{\beta} + (G_{\text{IIc}}w_{\tau}(d_{\tau}))^{\beta})^{1/\beta} \quad (29)$$

where  $\beta \geq 1$  and the  $w_i(d_i)$  are continuous, positive, increasing functions such that  $w_i(0) = 0$  and  $w_i(1) = 1$ . We then define the dissipation pseudo-potential for each interface as follows:

$$\phi(\dot{\boldsymbol{\alpha}}; \boldsymbol{\alpha}) = \frac{\partial \varphi}{\partial \boldsymbol{\alpha}} \cdot \dot{\boldsymbol{\alpha}} + I_{\mathbb{R}^+}(\dot{\boldsymbol{\alpha}}) = \overline{\varphi(\dot{\boldsymbol{\alpha}})} + I_{\mathbb{R}^+}(\dot{\boldsymbol{\alpha}}) \quad (30)$$

which is indeed convex and positively homogeneous with respect to  $\dot{\boldsymbol{\alpha}}$  and where  $I_{\mathbb{R}^+}$  is the indicator function corresponding to the damage irreversibility condition  $\dot{d}_{\nu}, \dot{d}_{\tau} \geq 0$ .

Such a choice corresponds to the following damage criterion:

$$\mathbf{Y} \leq \frac{\partial \varphi}{\partial \boldsymbol{\alpha}} \quad (31)$$

that is:

$$Y_{\nu} \leq (G_{\text{Ic}})^{\beta} w'_{\nu}(d_{\nu}) w_{\nu}(d_{\nu})^{\beta-1} S^{1/\beta-1} \quad (32)$$

$$Y_{\tau} \leq (G_{\text{IIc}})^{\beta} w'_{\tau}(d_{\tau}) w_{\tau}(d_{\tau})^{\beta-1} S^{1/\beta-1} \quad (33)$$

$$\text{where } S = (G_{\text{Ic}}w_{\nu}(d_{\nu}))^{\beta} + (G_{\text{IIc}}w_{\tau}(d_{\tau}))^{\beta} \quad (34)$$

This criterion implies:

$$\left(\frac{Y_{\nu}/w'_{\nu}(d_{\nu})}{G_{\text{Ic}}}\right)^{\gamma} + \left(\frac{Y_{\tau}/w'_{\tau}(d_{\tau})}{G_{\text{IIc}}}\right)^{\gamma} \leq 1 \quad (35)$$

with  $\gamma = \beta/(\beta - 1)$ .

Note that it is always possible to replace the damage variables  $\boldsymbol{\alpha} = (d_\nu, d_\tau)$  with  $\tilde{\boldsymbol{\alpha}} = (w_\nu(d_\nu), w_\tau(d_\tau))$ . In this case, the corresponding associated thermodynamic force from (24) reads:

$$\tilde{\mathbf{Y}} = -\frac{\partial \Psi}{\partial \tilde{\boldsymbol{\alpha}}} = -\frac{\partial \Psi}{\partial \boldsymbol{\alpha}} \frac{\partial \boldsymbol{\alpha}}{\partial \tilde{\boldsymbol{\alpha}}} \quad (36)$$

that is:

$$\tilde{Y}_\nu = \frac{Y_\nu}{w'_\nu(d_\nu)} \quad (37)$$

$$\tilde{Y}_\tau = \frac{Y_\tau}{w'_\tau(d_\tau)} \quad (38)$$

As a result, we recover from (35) the power-law delamination criterion (28) for:

$$G_I = \tilde{Y}_\nu = \frac{Y_\nu}{w'_\nu(d_\nu)} \quad (39)$$

$$G_{II} = \tilde{Y}_\tau = \frac{Y_\tau}{w'_\tau(d_\tau)} \quad (40)$$

Finally, in the case where  $\beta \rightarrow \infty$ , (29) becomes:

$$\varphi(\boldsymbol{\alpha}) = \max\{G_{Ic} w_\nu(d_\nu); G_{IIc} w_\tau(d_\tau)\} \quad (41)$$

and is associated with the linear criterion  $\frac{G_I}{G_{Ic}} + \frac{G_{II}}{G_{IIc}} \leq 1$ . Similarly, if  $\beta = 1$ , (29) reads:

$$\varphi(\boldsymbol{\alpha}) = G_{Ic} w_\nu(d_\nu) + G_{IIc} w_\tau(d_\tau) \quad (42)$$

and we recover a delamination criterion with no mixed-mode interaction:  $G_I \leq G_{Ic}$  and  $G_{II} \leq G_{IIc}$ .

#### 4.2. Incremental variational principle

The system evolution equation between time  $t_n$  and  $t_{n+1}$  is then obtained by resorting to the minimization of the incremental potential for rate-independent systems [45–47]:

$$(\mathbf{U}_{n+1}, \mathbf{d}_{n+1}) = \arg \min_{\mathbf{U}, \mathbf{d}} \mathcal{E}_n(\mathbf{U}, \mathbf{d}) \quad (43)$$

where the energy potential on this load increment is given as the sum of the potential energy and a dissipated contribution by:

$$\mathcal{E}_n(\mathbf{U}, \mathbf{d}) = \mathcal{E}_{\text{pot}}(\mathbf{U}, \mathbf{d}) + \mathcal{D}_n(\mathbf{d}) \quad (44)$$

$$\mathcal{E}_{\text{pot}}(\mathbf{U}, \mathbf{d}) = \int_\omega \Psi(\mathbf{E}, \mathbf{d}) \, d\omega - \mathcal{W}_{\text{ext}}(\mathbf{U}) \quad (45)$$

$$\mathcal{D}_n(\mathbf{d}) = \int_\omega \int_{t_n}^{t_{n+1}} \Phi(\dot{\mathbf{d}}; \mathbf{d}) \, dt \, d\omega \quad (46)$$

with  $\mathcal{W}_{\text{ext}}$  being the work of external loads. With  $\Phi$  given by (23) and (30), we get:

$$(\mathbf{U}_{n+1}, \mathbf{d}_{n+1}) = \arg \min_{\mathbf{U}, \mathbf{d} \geq \mathbf{d}_n} \mathcal{E}_n(\mathbf{U}, \mathbf{d}) \quad (47)$$

$$\text{with } \mathcal{D}_n(\mathbf{d}) = \sum_{m=1}^n \int_{\omega} \varphi(\boldsymbol{\alpha}^m) d\omega \quad (48)$$

where the irreversibility condition  $\dot{\mathbf{d}} \geq 0$  has been transformed into the incremental condition  $\mathbf{d} \geq \mathbf{d}_n$  and where we dropped the constant term in  $\varphi(\boldsymbol{\alpha}_n^m)$  at time  $t_n$  in the expression for  $\mathcal{D}_n$  since it does not impact the energy minimization.

## 5. Damage-dependent elastic energy

In this section, we discuss our modeling of the damage-dependent elastic energy  $\Psi(\mathbf{E}, \mathbf{d})$  by first considering the simple case of only one damageable interface.

### 5.1. The special case of a single delaminated interface

Let us consider here that only one interface can delaminate. In section 2.2, we detailed the derivation of the generalized out-of-plane  $\mathbb{C}_\nu^d$  and  $\mathbb{C}_\tau^d$  stiffness matrix in presence of one delaminated interface for the original LS1 model. In this single interface case, we propose to consider the following simple interpolation between the sound and the delaminated stiffness:

$$\mathbb{C}^\nu(d_\nu) = g(d_\nu)\mathbb{C}^\nu + (1 - g(d_\nu))\mathbb{C}_\nu^d \quad (49)$$

$$\mathbb{C}^\tau(d_\tau) = g(d_\tau)\mathbb{C}^\tau + (1 - g(d_\tau))\mathbb{C}_\tau^d \quad (50)$$

where  $g(d)$  is a positive decreasing function such that  $g(0) = 1$  and  $g(1) = 0$  characterizing the stiffness degradation.

### 5.2. The multi-interface case

In the general situation in which  $p$  different interfaces can delaminate, the generalization of the above procedure is not practical when  $p$  is large since it would rely on proposing an interpolation between the sound state and the  $2^p$  different delamination configurations and their associated stiffness matrices.

In the general case, we therefore propose to rely on the "lumped" LS1 model derived in section 3 which benefits from a diagonal stiffness matrix. We then naturally consider the following damage-dependent out-of-plane and shear stiffness matrices:

$$\mathbb{C}^\nu(d_\nu) = \text{diag}(g(d_\nu^{i,i+1})c_\nu^{i,i+1}) \quad (51)$$

$$\mathbb{C}^\tau(d_\tau) = \text{diag}(\bar{c}_\tau^1, g(d_\tau^{1,2})c_\tau^{1,2}, \bar{c}_\tau^2, \dots, g(d_\tau^{n-1,n})c_\tau^{n-1,n}, \bar{c}_\tau^n) \quad (52)$$

where we remark that the stiffnesses  $\bar{c}_\tau^i$  corresponding to the mid-ply shear stress are not degraded as we do not consider intra-ply delamination mechanisms. Let us also point out that (51)-(52) coincide with (49)-(50) when replacing  $\mathbb{C}^\nu$  and  $\mathbb{C}^\tau$  with the corresponding lumped stiffness matrices.

### 5.3. Modelling choices

In addition to the damage-dependent elastic stiffness described above, we also enhanced the elastic energy with a bound constraint  $\mathbf{d} \leq 1$  on the damage variable.

Specific instances of the proposed layerwise damage model are hence characterized by three distinct choices:

- the mixed-mode delamination exponent  $\beta$  (or, equivalently,  $\gamma$ )
- the dissipated energy density functions  $w_\nu(d_\nu)$  and  $w_\tau(d_\tau)$
- the stiffness degradation function  $g(d)$

In the following, we will consider:

$$g(d) = (1 - d)^p \quad (53)$$

$$w_i(d_i) = d_i^2 \quad i = \nu, \tau \quad (54)$$

Our model is therefore characterized by the mixed mode exponent  $\beta$  and the  $p$ -exponent.

The opening behaviour of a generic interface, omitting the interface index exponent for the sake of simplicity, can be written as  $\nu = g(d_\nu)c_\nu\varepsilon^\nu$  where  $c_\nu$  is the corresponding interface opening stiffness and  $\varepsilon_\nu$  the corresponding opening strain. Writing down the corresponding damage evolution criterion gives the following damage-dependent stress evolution:

$$\nu(d) = 2\sqrt{\frac{G_{Ic}c_\nu}{p}}\sqrt{d}(1-d)^{p+1} \quad (55)$$

from which we deduce the corresponding expressions for the maximal opening stress:

$$\nu_{\max} = \begin{cases} \frac{4}{3\sqrt{3}}\sqrt{G_{Ic}c_\nu} & \text{for } p = 1 \\ \frac{9}{8\sqrt{6}}\sqrt{G_{Ic}c_\nu} & \text{for } p = 2 \end{cases} \quad (56)$$

We see that the model with  $p = 2$  therefore produces a smaller maximum opening stress than for the model with  $p = 1$ . The corresponding stress-deformation curves have been reported in Figure 4. We can see that the  $p = 1$  exhibits a much more brittle behaviour with a finite deformation for which the stress vanishes whereas the  $p = 2$  model is more progressive, the stress vanishing only asymptotically for  $\varepsilon_\nu \rightarrow \infty$ .

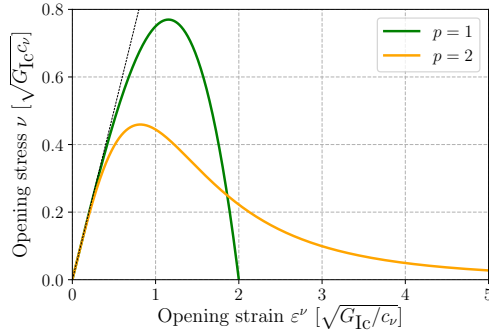


Figure 4: Interface behaviour in pure opening mode

Finally, we see that these maximum stresses are completely determined by the the interface fracture energy  $G_{Ic}$  and the interface stiffness  $c_\nu$ , which depends on the surrounding ply thickness and elastic properties. As a result, these models cannot account for an independent value of the interface critical stress which would be, for instance, measured from the bonding material tensile strength. In general, interfacial bond strengths are much lower than the critical stress computed from (56).

To overcome this issue, the previous models can be generalized by considering, for instance, the following fracture energy densities:

$$w_i(d_i) = \frac{(\kappa_i - 1)d_i^2}{\kappa_i - d_i^2} \quad \text{for } i = \nu, \tau \quad (57)$$

which involve two additional non-dimensional parameters  $\kappa_\nu, \kappa_\tau > 1$ . Note that, in the limit case  $\kappa_i \rightarrow \infty$ , the previous model  $w_i(d_i) = d_i^2$  is retrieved. The choice of  $\kappa_i$  will influence the value of the corresponding maximum opening/shear stress which can range between 0 and the value given by (56) for  $\kappa_i$  ranging from 1 and  $+\infty$ . No closed form expression of  $\kappa_i$  as a function of the maximum stress is available but the corresponding relation can be solved numerically as detailed in Appendix A.6.

Finally, let us conclude by saying that other choices leading to other stress-deformation curves are possible, following for instance the work of Wu [48].

## 6. Numerical implementation

### 6.1. Finite-element discretization

The weak form of the LS1 model multilayered plate model has been implemented in the open-source finite element FEniCS package [49, 50] using quadratic triangular elements for all kinematical variables and selective reduced integration on the shear part of the strain energy to remove shear-locking as in classical Reissner-Mindlin models [51]. In the following, damage is represented as an element-wise constant field and computed using a single quadrature point rule.

### 6.2. Nonlinear damage problem resolution

In order to solve the nonlinear system arising from the incremental variational problem (47), we rely on a staggered algorithm which consists in alternate minimization on the displacement  $\mathbf{U}$  at fixed damage and on the damage  $\mathbf{d}$  at fixed displacement, until reaching convergence on a given load step. This approach offers high robustness, especially during unstable delamination propagation phases, at the expense of a larger number of iterations compared to Newton-like methods. This approach is widely used in phase-field models of brittle fracture [52–55] and can benefit from various acceleration strategies, including Anderson acceleration [56, 57], over-relaxation [57, 58], etc.

This alternate minimization strategy therefore requires the resolution of two single-field minimization sub-problems:

- minimization with respect to  $\mathbf{U}$  corresponds to a linear elasticity problem at fixed  $\mathbf{d}$ .
- minimization with respect to  $\mathbf{d}$  results in a nonlinear minimization problem with bound constraints  $\mathbf{d}_n \leq \mathbf{d} \leq 1$  accounting for both the incremental irreversibility and the bounded damage constraint included in the stored energy density.

The latter problem is in fact of pure local nature (with respect to the in-plane discretization) and can be solved at the material point-level using a local non-linear solver in general. In addition, due to the diagonal form (51)-(52) of the damage-dependent stiffness matrix, each interfacial damage problem is decoupled from one another. Only  $d_\nu^{i,i+1}$  and  $d_\tau^{i,i+1}$  are coupled by the mixed-mode criterion, except in the case  $\beta = 1$  where the opening and sliding damage problems decouple from each other.

### 6.3. Taking into account tension/compression asymmetry

In the model description of the previous sections, opening damage could occur either in tension or in compression. To avoid unphysical damage in compression, one could split the stored energy into a positive and negative part with respect to the sign of the interface opening strains. This would make the  $\mathbf{U}$ -minimization sub-problem nonlinear, incurring additional computational cost. Instead, we made the choice of a hybrid strategy, akin to that of [54], where this positive/negative split of the energy is considered only when evaluating the damage criterion i.e.  $\mathbf{Y} = -\frac{\partial \Psi^+}{\partial \mathbf{d}}$  where  $\Psi^+ = \frac{1}{2} \mathbf{E}^{\text{el},+} \mathbb{C}(d) \mathbf{E}^{\text{el},+}$  with  $\mathbf{E}^{\nu, \text{el},+} = \langle \mathbf{E}^{\nu, \text{el}} \rangle_+$  for the opening strains associated with  $\nu^{i,i+1}$  and  $\mathbf{E}^{\text{el},+} = \mathbf{E}^{\text{el}}$  otherwise.

Moreover, to prevent layers interpenetration in compression, the opening damage variable  $d_\nu$  are momentarily set to 0 if the corresponding strain is negative and restored to its previous value when the strain is positive.

#### 6.4. Opening and sliding fracture coupling

With the current formulation, introducing two damage variables representing opening and sliding modes enables to describe independently the damage evolution process for both modes while coupling both of them through the power-law interaction criterion. However, upon full fracture ( $d = 1$ ), this strategy can lead to an independent evolution between two distinct “opening” and “sliding” delamination fronts, which is clearly non-physical. This problem has been mentioned by [5]. In this work, we use the approach proposed by [59] which consists in imposing  $d_\nu = d_\tau$  as soon as one variable reaches a value  $d_c \approx 1$ .

### 7. Validation and illustrative delamination examples

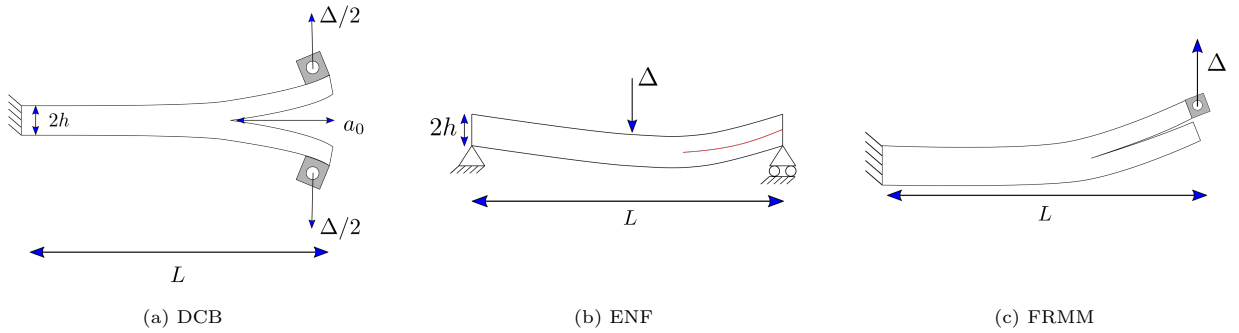


Figure 5: Geometry of the considered delamination tests

We will now validate our modelling strategy against pure and mixed mode delamination tests. Comparisons with analytical solutions will be carried out on an isotropic beam of with the following mechanical properties:  $E = 70 \text{ GPa}$ ,  $\nu = 1/3$ ,  $G_{Ic} = G_{IIc} = 1 \text{ J/m}^2$ . The beam length is  $L = 200 \text{ mm}$  and both arms have a thickness of  $h = 6 \text{ mm}$  each. In the subsequent sections, the comparison with simple tests analytical solutions will be done in the linear elastic fracture mechanics (LEFM) setting. As a result, we will, from now on and until further notice, consider a damage model without any critical stress, that is  $\kappa_\nu, \kappa_\tau \rightarrow \infty$ .

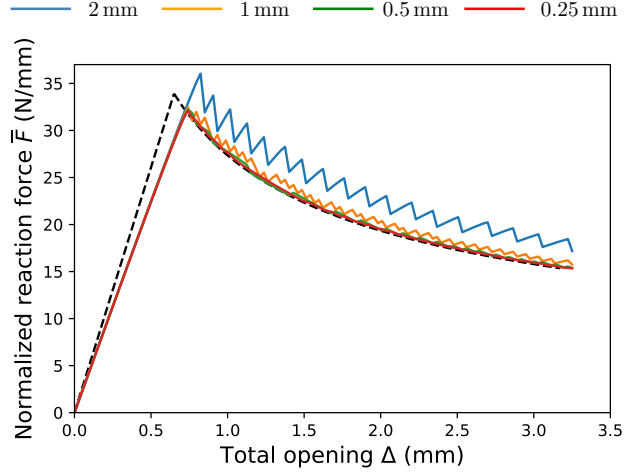
#### 7.1. Double Cantilever Beam

We first validate our model on the classical mode I Double Cantilever Beam (DCB) test. A vertical displacement  $\pm\Delta/2$  is prescribed at the end of a specimen containing an initial pre-crack of length  $a_0$  (see Figure 5a). Using a Timoshenko beam model in the LEFM setting, the vertical displacement and the reaction force are related by the following analytical formula [60]:

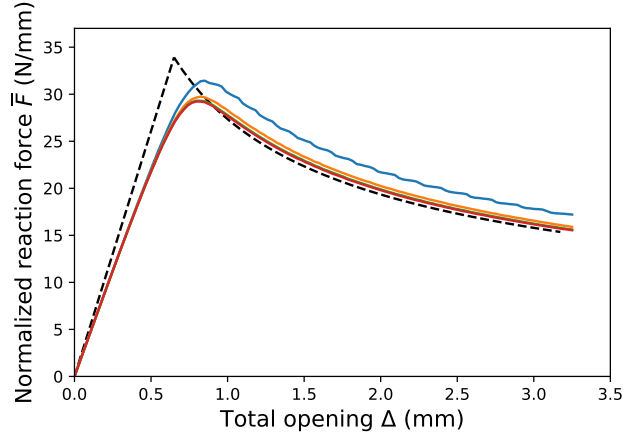
$$\Delta(F) = \frac{2Fa_0^3}{3EI} \left( 1 + \frac{3EI}{a_0^2\mu A_s} + \frac{3}{a_0} \sqrt{\frac{EI}{\mu A_s}} \right), \quad (58)$$

$$F \leq F_{\max} = \frac{\sqrt{EIbG_c}}{a_0 + \sqrt{\frac{EI}{\mu A_s}}} \quad (59)$$

where  $F_{\max}$  denotes the critical applied force corresponding to the onset of delamination,  $b$  is the beam width,  $A_s$  the effective cross-section of one arm  $A_s = 5A/6 = 5(bh)/6$ ,  $I = bh^3/12$  is its area moment of inertia and finally  $\mu$  is the shear modulus. As the crack advances to a current length  $a$ , the above expressions are simply updated by replacing  $a_0$  with  $a$ . Note that more advanced analytical expressions taking into account elastic foundation effects can also be found in [61, 62].



(a)  $p = 1$  damage model



(b)  $p = 2$  damage model

Figure 6: Load-displacement curve  $\bar{F}(\Delta)$  for two damage models and various mesh sizes, dashed line: LEFM analytical solution.

Figure 6 displays the obtained load-displacement curves  $\bar{F}(\Delta)$  for two damage models with exponent  $p = 1$  or  $p = 2$  and various uniform mesh sizes. As expected, the  $p = 1$  model (Figure 6a) yields an almost brittle behaviour, that is the occurrence of an elastic phase before the onset of delamination. Clearly, we obtain a satisfying mesh convergence to the LEFM solution, with coarse meshes leading to load-displacement oscillations in the propagation phase due to local unstable propagation on a single element. The  $p = 2$

damage model (Figure 6b) exhibits a very satisfying mesh convergence and a smoother overall behaviour. Indeed, due to its different stress-deformation curve (see again Figure 4), damage is evolving slowly at low load levels, which tends to smoothen the stress peak and oscillations for coarse meshes. Finally, we can highlight that both models yield a smaller initial elastic stiffness. This slight deviation can be attributed to the large aspect ratio of both arms in the pre-cracked configurations which enhances the differences between the LS1 numerical solutions and the Timoshenko beam analytical solution of [60].

Secondly, comparison between the lumped LS1 model (51)-(52) and its consistent version (49)-(50) is illustrated on Figure 7 for for a mesh size of 1 mm. One can notice that the differences between both model predictions are extremely small. In particular, even if the diagonal compliance term in (12) increases by 25% when considering the lumped expression (13), its impact on the global elastic slope is completely negligible for this problem. A small difference in the peak load can be observed but both models are very close to each other in the propagation phase. As a result, all forthcoming simulations will be conducted using the lumped LS1 model.

Finally, we test the DCB problem with the critical-stress dependent model (56) by varying the critical stress  $\sigma_\nu^c$  and thus  $\kappa_\nu$ . Results are represented in Figure 8 for  $\sigma_\nu^c \in [20, 30, 40, 50]$  MPa. As expected, for smaller  $\sigma_\nu^c$ , the maximum load is smaller with a much flatter peak with all curves converging to the LEFM solution in the full propagation phase.

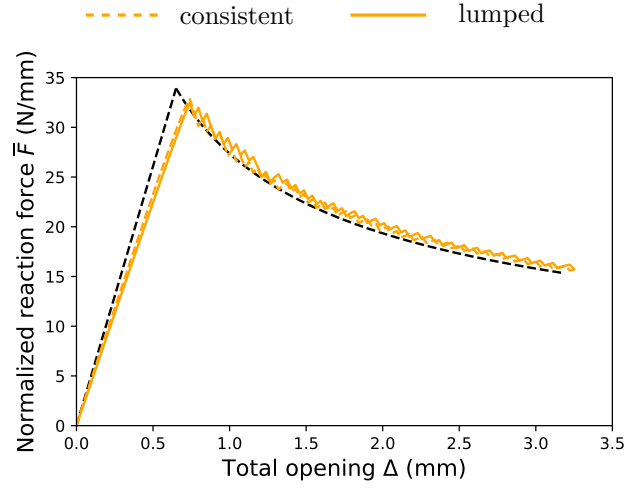
## 7.2. End Notched Flexure

The End Notched Flexure (ENF) test is a mode II failure test, as illustrated in Figure 5b. For an Euler-Bernoulli beam model, closed-form relation between the vertical displacement and the applied force are available in [63]. Again, refined expressions can be found in [61, 64].

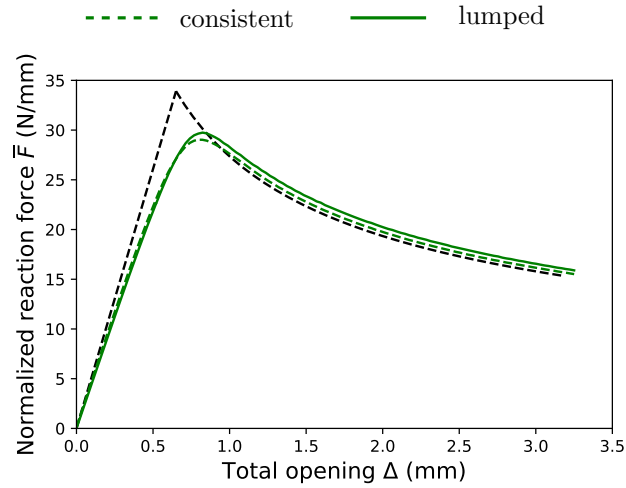
Contrary to the DCB test which always results in a stable propagation with displacement-control, the ENF test leads to a stable propagation only if  $a_0 \geq 0.327L = 65.4$  mm [63]. We therefore compare our results with two different pre-crack lengths,  $a_0 = 80$  mm or  $a_0 = 40$  mm which should lead to either a stable or unstable propagation respectively.

Figure 9 displays the load-displacement curves of the two damage models for a uniform mesh size of 1 mm. Once again, the results are quantitatively very satisfactory, both models reproducing the loss of stability depending on the initial crack length  $a_0$ . Again, the quadratic  $p = 2$  model smoothes the peak load which also leads to an earlier onset of the unstable propagation phase in the case  $a_0 = 80$  mm. At the expense of a large number of iterations, the staggered alternate minimization algorithm enabled to reach the new equilibrium but without any convergence problem.

Finally, similarly to the pure mode I DCB test, the  $\beta$  exponent characterizing the mixed-mode propagation criterion has no impact on this pure mode II test.



(a)  $p = 1$  damage model



(b)  $p = 2$  damage model

Figure 7: Load-displacement curve  $\bar{F}(\Delta)$  obtained with the consistent or lumped LS1 model, dashed line: LEFM analytical solution.

### 7.3. Mixed-mode delamination

We now turn to a mixed-mode delamination test for which crack propagation occurs when the total energy release rate  $G$  reaches a critical value  $G_c$  which depends on the mode mixity ratio  $\theta = G_I/G_{II}$  and on the chosen mixed-mode interaction criterion.

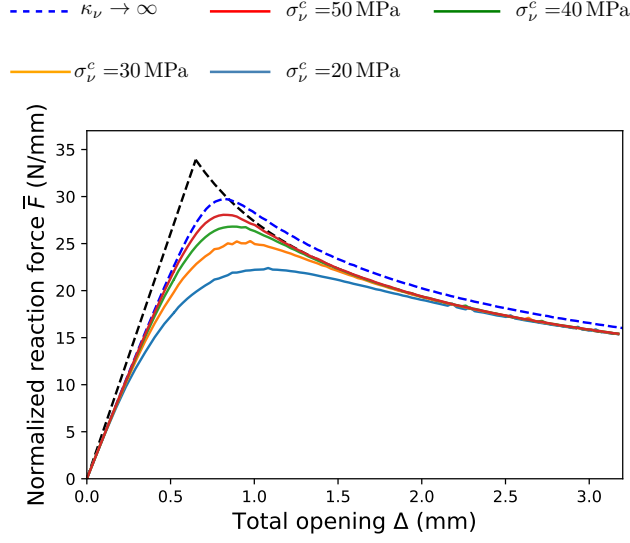


Figure 8:  $p = 2$ , Load-displacement curve for various critical out-of-plane stress  $\sigma_c$ , mesh size 1 mm

For the power-law criterion considered in this work, we have during propagation:

$$G_I + G_{II} = G \quad (60a)$$

$$\left(\frac{G_I}{G_{Ic}}\right)^\gamma + \left(\frac{G_{II}}{G_{IIc}}\right)^\gamma = 1 \quad (60b)$$

$$G_I = \theta G_{II} \quad (60c)$$

The effective total critical energy restitution rate  $G_c(\theta)$  during propagation at fixed mode mixity is therefore given by:

$$G_c(\theta) = \frac{(1 + \theta)}{\left(\left(\frac{\theta}{G_{Ic}}\right)^\gamma + \left(\frac{1}{G_{IIc}}\right)^\gamma\right)^{1/\gamma}} \quad (61)$$

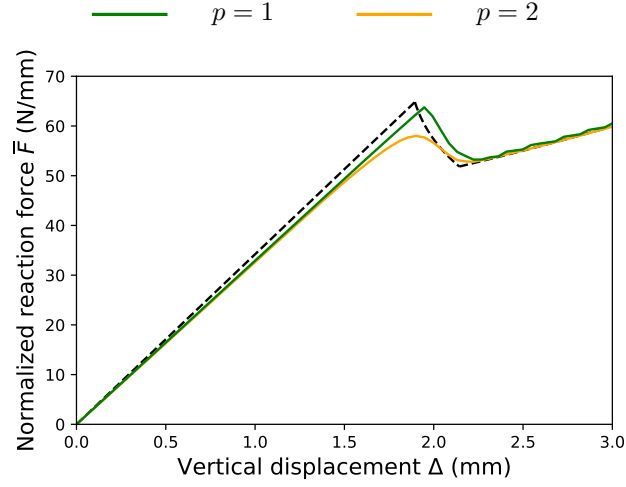
The Fixed Ratio Mixed Mode (FRMM) test which we now consider, is precisely a mixed mode test resulting in a constant mode mixity of  $\theta = 4/3$  throughout the whole test. It is akin to a DCB test in which the displacement is applied to one arm only, see Figure 5c. The analytical solution for an Euler-Bernoulli beam model [65] reads:

$$\Delta(F) = \frac{L^3 + 7a^3}{3EI_{tot}} F \quad (62)$$

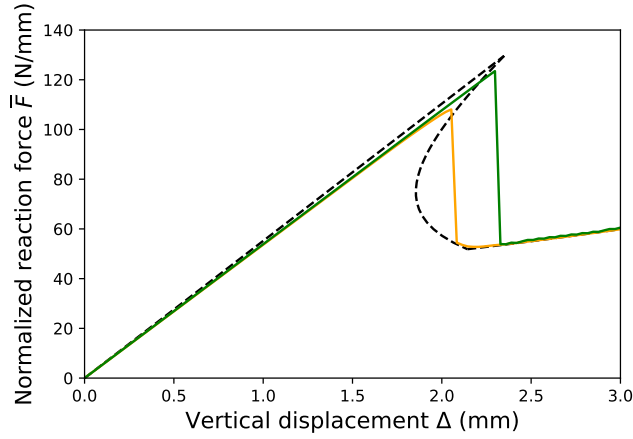
$$\text{with } \begin{cases} a = a_0 & \text{before propagation} \\ a = \left(\frac{2bEI_{tot}G_c}{7F^2}\right)^{1/2} & \text{during propagation} \end{cases} \quad (63)$$

where  $I_{tot} = b(2h)^3/12$  is the beam total second moment of area .

Similarly to the ENF test, for a sufficiently small pre-crack ( $a_0 \leq 0.415L = 83$  mm), LEFM predicts an unstable propagation. Figure 10 displays the results obtained during a stable test with  $a_0 = 120$  mm



(a)  $a_0 = 80$  mm (stable propagation)



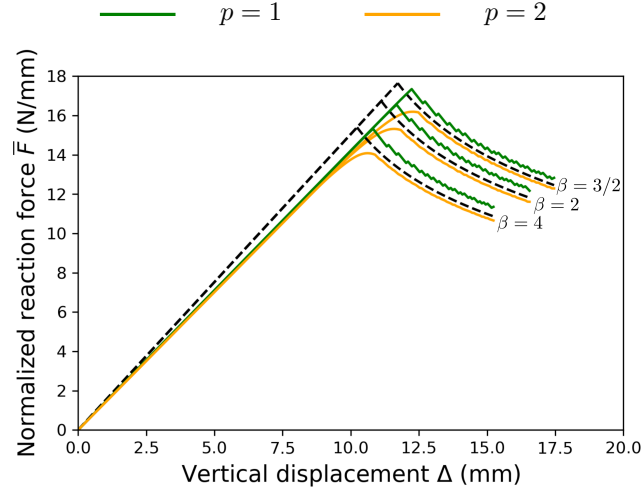
(b)  $a_0 = 40$  mm (unstable propagation)

Figure 9: Load-displacement curve of the ENF test for both damage models and two pre-crack lengths, dashed line: LEFM analytical solution.

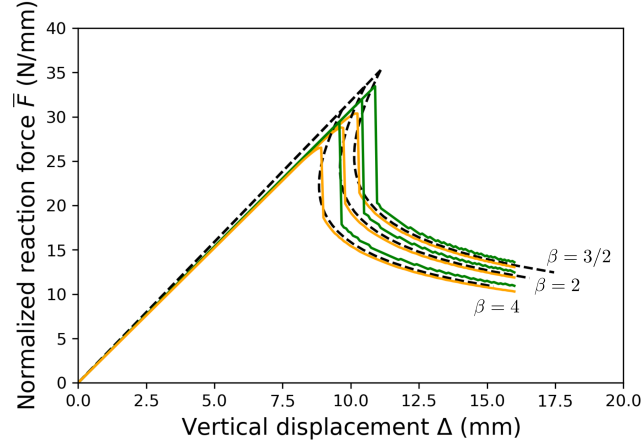
and an unstable test with  $a_0 = 80$  mm. Again, the quantitative comparison is excellent. The stress peak is correctly evaluated and the softening phase is well reproduced. The mixed-mode exponent  $\beta$  has a strong influence on these two points, so that the accuracy of our two numerical curves highlights that the elliptic interpolation induced by our coupled cracking energy density is correct.

#### 7.4. Multi-interfaces failure

We now consider the multi-interface delamination experimental test introduced by [66] and reproduced numerically in [5], [67]. It consists in a DCB with two initial delaminated regions on two different interfaces (see figure 11). Despite both failure modes are activated in this test, it is essentially mode I dominated so that the  $\beta$  exponent of the interaction criterion plays only a little role here. The considered beam is a



(a)  $a_0 = 120$  mm (stable propagation) for various  $\beta$  exponents.



(b)  $a_0 = 80$  mm (unstable propagation)

Figure 10: Force-displacement curve force for two pre-crack lengths.

laminate of 24 unidirectional  $0^\circ$  plies with parameters given in Table 2 [66]. In our implementation, the laminate is modelled as three effective plies consisting respectively of 10, 2 and 12 UD layers.

Figure 12 displays the load-displacement curve obtained with our model. The final deformed configuration involving important delaminations of both interfaces has been represented in Figure 13. Overall, our results match the phenomenology of the experimental test very well, with only a minor difference as regards the different propagation phases. Indeed, similarly to the numerical model of [67], our model predicts two instabilities. The first stress drop ② corresponds to the unstable propagation of the rightmost crack until reaching the tip of the second one. The second stress-drop ③ corresponds to a small unstable propagation of the top crack only (Figure 14c). Finally, phase ④ corresponds to a stable propagation phase of both cracks, the bottom one advancing faster than the top one. Finally, note that the second unstable phase ③

Material parameters		
$E_L = 115 \text{ GPa}$	$E_T = 9.5 \text{ GPa}$	$\nu_{TN} = 0.3$
$G_{LT} = G_{TN} = G_{LN} = 4.5 \text{ GPa}$	$\nu_{LT} = \nu_{LN} = 0.29$	
$G_{Ic} = 330 \text{ J m}^{-2}$	$G_{IIc} = 800 \text{ J m}^{-2}$	

Table 2: Material parameters for the multi-interface DCB test

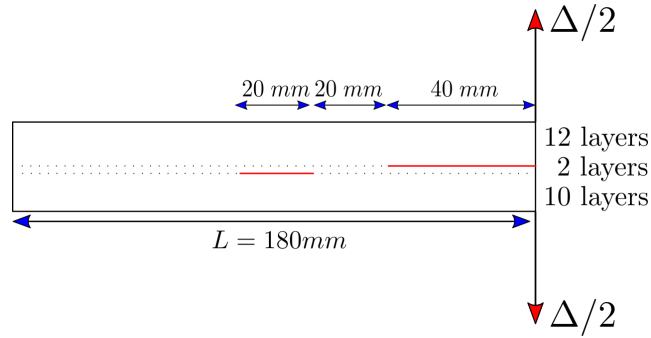


Figure 11: Multi-interface Double Cantilever Beam geometry

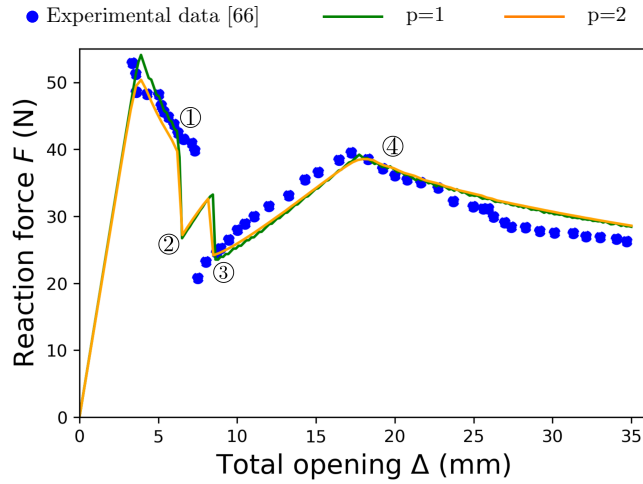


Figure 12: Load-displacement curve for the multi-interface DCB test

is not observed in the experiments but has also been reported numerically in [67]. As seen in Figure 12, the quantitative agreement with the experimental load-displacement curve is very good.

## 8. Conclusions and perspectives

In this work, we considered a stress-based layerwise plate model and its extension towards delamination modelling. Continuous damage mechanics has been used to formulate a damage-dependent layerwise model.

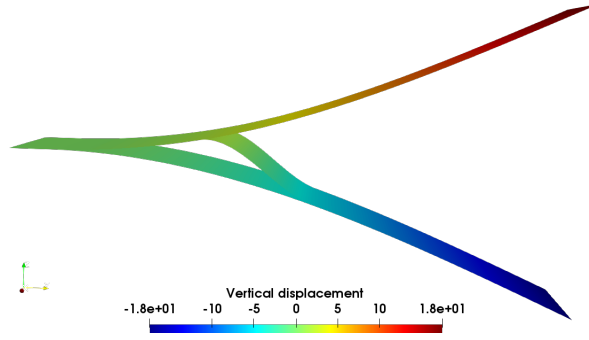


Figure 13: Final deformed configuration ( $\times 2$ ) for the multi-interface DCB test.

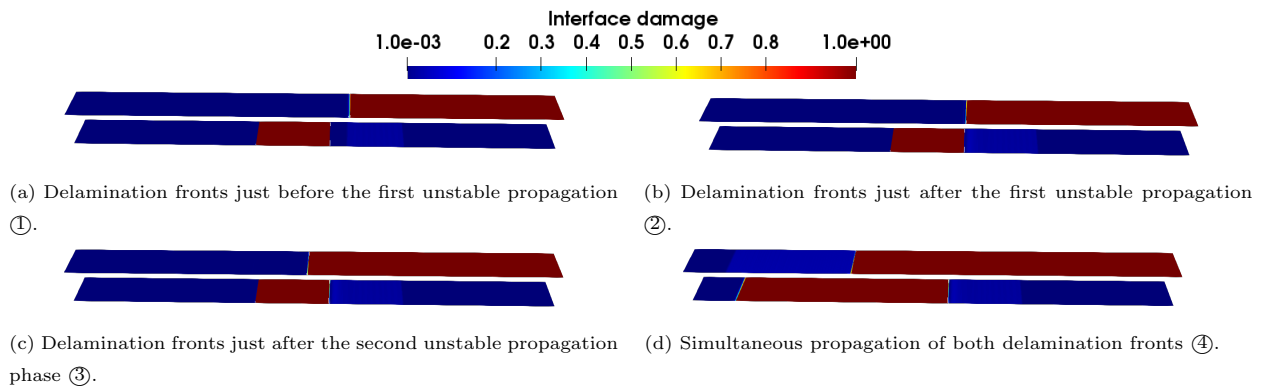


Figure 14: Delamination fronts on both interfaces during the multi-interface DCB test.

A simplified expression of the original layerwise model, akin to mass-lumping procedures in dynamics, enabled us to obtain a much simpler formulation, avoiding complex coupling between the various plies in the laminate global stiffness matrix. The variational character of the mechanical problem is ensured by the generalized standard media theory. In this framework, a coupled dissipation potential has been proposed to take into account the coupling of the failure modes at the interface. Many classical benchmarks have been run to validate our approach. Numerical simulations show a very good agreement with respect to reference solutions. A multi-interface cracking test illustrated the excellent capabilities of our model to reproduce non-trivial damage kinetics.

A natural continuation of this work concerns its extension to intra-laminar failure mechanisms such as fiber breakage and matrix cracking. Damage modeling of ply failure mechanisms is more challenging due to the potential occurrence of damage localization. Local ply damage models must therefore be regularized to avoid any mesh-dependency issue. In this regard, phase-field approaches of brittle fracture seem promising and would easily fit into the current variational and numerical framework. Interaction between delamination

and ply failure would therefore be worthy to investigate in order to enhance the LS1 model capabilities to simulate failure phenomena fully in layered structures. In particular, investigation of failure patterns caused by low-velocity impacts is particularly challenging due to the strong interplay between the various failure mechanisms.

## 9. Acknowledgements

The authors would like to thank Dassault Aviation for supporting this work.

## Appendix A. LS1 layerwise model

### Appendix A.1. Notations and hypotheses

- On the lateral part  $\partial\Omega_D$ , homogeneous Dirichlet boundary conditions are applied
- The plate is loaded on the upper  $\omega^+$  and lower  $\omega^-$  surface, gathered under the notation  $\partial\Omega_N$ , with a force distribution  $\mathbf{T}^+ = (T_k^+)$  and  $\mathbf{T}^- = (T_k^-)$  respectively. Body forces are neglected.
- The Greek subscript  $\alpha, \beta, \gamma, \delta$  designate the in-plane components and take their values in  $\llbracket 1; 2 \rrbracket$ . The Latin indices  $i, j$  designates the general components and take the values  $\llbracket 1; 3 \rrbracket$ .
- Einstein's summation convention is used.
- Small strain hypothesis is retained.

### Appendix A.2. LS1 stress field

We postulate that in each layer, the membrane stress field is written  $\forall (x_1, x_2) \in \omega, x_3 \in [h_i^-, h_i^+]$ :

$$\sigma_{\alpha\beta}^{i,3D}(x_1, x_2, x_3) = N_{\alpha\beta}^i(x_1, x_2) \frac{P_0^i(x_3)}{e^i} + M_{\alpha\beta}^i(x_1, x_2) \frac{12P_1^i(x_3)}{e^{i2}} \quad (\text{A.1})$$

where we make use of the polynomial basis  $P_k^i(x_3) := L_k\left(\frac{x_3 - \bar{h}_i}{e^i}\right)$  built from Legendre polynomials:

$$L_0(y) = 1; L_1(y) = y; L_2(y) = -6y^2 + \frac{1}{2}; L_3(y) = -2y^3 + \frac{3}{10}y$$

In order to satisfy the local 3D balance equations, the out-of-plane shear stress must necessarily be quadratic and the out-of-plane normal stress must be cubic with respect to  $x_3$ . Taking into account the continuity of the stresses  $\sigma_{\alpha 3}^{i,3D}(x_1, x_2, x_3)$  and  $\sigma_{33}^{i,3D}(x_1, x_2, x_3)$  at the interfaces between the layers, it can

be easily established that such stress fields have the following expressions in layer  $i$ :

$$\begin{aligned}\sigma_{\alpha 3}^{i,3D} &= Q_{\alpha}^i(x_1, x_2) \frac{P_0^i(x_3)}{e^i} + [(\tau_{\alpha}^{i,i+1} - \tau_{\alpha}^{i-1,i})(x_1, x_2)] P_1^i(x_3) \\ &+ \left[ Q_{\alpha}^i - \frac{e^i}{2} (\tau_{\alpha}^{i,i+1} + \tau_{\alpha}^{i-1,i})(x_1, x_2) \right] \frac{P_2^i(x_3)}{e^i}\end{aligned}\quad (\text{A.2})$$

$$\begin{aligned}\sigma_{33}^{i,3D} &= \left[ \left( \frac{1}{2} (\nu^{i,i+1} + \nu^{i-1,i}) + \frac{e^i}{12} (\tau_{\alpha}^{i,i+1} - \tau_{\alpha}^{i-1,i}) \right) (x_1, x_2) \right] P_0^i(x_3) \\ &+ \left[ \left( \frac{e^i}{10} (\tau_{\alpha}^{i,i+1} + \tau_{\alpha}^{i-1,i}) + \frac{6}{5} (\nu^{i,i+1} - \nu^{i-1,i}) \right) (x_1, x_2) \right] P_1^i(x_3) \\ &+ \left[ \left( \frac{e^i}{12} (\tau_{\alpha}^{i,i+1} - \tau_{\alpha}^{i-1,i}) \right) (x_1, x_2) \right] P_2^i(x_3) \\ &+ \left[ \left( \frac{e^i}{2} (\tau_{\alpha}^{i,i+1} + \tau_{\alpha}^{i-1,i}) + (\nu^{i,i+1} - \nu^{i-1,i}) \right) (x_1, x_2) \right] P_3^i(x_3)\end{aligned}\quad (\text{A.3})$$

where the introduced generalized stresses are related by the generalized balance equations (3a)–(3c).

### Appendix A.3. Generalized strain measures

The generalized strain measures respectively associated with the generalized stresses  $\mathbf{N}^i$ ,  $\mathbf{M}^i$ ,  $\mathbf{Q}^i$ ,  $\boldsymbol{\tau}^{j,j+1}$  and  $\nu^{j,j+1}$  are given as follows in terms of the generalized displacements:

$$\begin{aligned}\boldsymbol{\varepsilon}^i &= \frac{1}{2} \left( \mathbf{grad}(\mathbf{U}^i) + \mathbf{grad}^{\top}(\mathbf{U}^i) \right) \\ \boldsymbol{\chi}^i &= \frac{1}{2} \left( \mathbf{grad}(\boldsymbol{\Phi}^i) + \mathbf{grad}^{\top}(\boldsymbol{\Phi}^i) \right) \\ \boldsymbol{\gamma}^i &= \boldsymbol{\Phi}^i + \mathbf{grad}(U_3^i) \\ \mathbf{D}^{j,j+1} &= \mathbf{U}^{j+1} - \mathbf{U}^j - \frac{e^{j+1}}{2} \boldsymbol{\Phi}^{j+1} - \frac{e^j}{2} \boldsymbol{\Phi}^j \\ \varepsilon_{\nu}^{j,j+1} &= U_3^{j+1} - U_3^j\end{aligned}\quad (\text{A.4})$$

In the following, we adopt Voigt's notation for the generalized stress and the associated strain:

$$\mathbf{E}^{\top} = \{ \mathbf{E}^{K,\top}, \mathbf{E}^{\nu,\top}, \mathbf{E}^{Q,\top} \} \quad \boldsymbol{\Sigma}^{\top} = \{ \boldsymbol{\Sigma}^{K,\top}, \boldsymbol{\Sigma}^{\nu,\top}, \boldsymbol{\Sigma}^{Q,\top} \}$$

$$\begin{aligned}\mathbf{E}^{K,\top} &= \{ \varepsilon_{11}^1, \varepsilon_{22}^1, 2\varepsilon_{12}^1, \chi_{11}^1, \chi_{22}^1, 2\chi_{12}^1, \dots, \\ &\dots, \varepsilon_{11}^n, \varepsilon_{22}^n, 2\varepsilon_{12}^n, \chi_{11}^n, \chi_{22}^n, 2\chi_{12}^n \}\end{aligned}\quad (\text{A.5})$$

$$\mathbf{E}^{\nu,\top} = \{ \varepsilon_{\nu}^{1,2}, \dots, \varepsilon_{\nu}^{n-1,n} \} \quad (\text{A.6})$$

$$\mathbf{E}^{Q,\top} = \{ \gamma_1^1, \gamma_2^1, D_1^{1,2}, D_2^{1,2}, \dots, D_1^{n-1,n}, D_2^{n-1,n}, \gamma_1^n, \gamma_2^n \} \quad (\text{A.7})$$

$$\begin{aligned}\boldsymbol{\Sigma}^{K,\top} &= \{ N_{11}^1, N_{22}^1, N_{12}^1, M_{11}^1, M_{22}^1, M_{12}^1, \dots, \\ &\dots, N_{11}^n, N_{22}^n, N_{12}^n, M_{11}^n, M_{22}^n, M_{12}^n \}\end{aligned}\quad (\text{A.8})$$

$$\boldsymbol{\Sigma}^{\nu,\top} = \{ \nu^{1,2}, \dots, \nu^{n-1,n} \} \quad (\text{A.9})$$

$$\boldsymbol{\Sigma}^{Q,\top} = \{ Q_1^1, Q_2^1, \tau_1^{1,2}, \tau_2^{1,2}, \dots, \tau_1^{n-1,n}, \tau_2^{n-1,n}, Q_1^n, Q_2^n \} \quad (\text{A.10})$$

in which the exponents  $K, \nu, Q$ , respectively refer to the generalized Kirchhoff stress/strain, the generalized out-of-plane stress/strain and the generalized shear stress/strain (both intra and inter-laminar).

*Appendix A.4. Compliance matrix*

The generalized compliance matrix of the laminate has a diagonal block structure:

$$\mathbb{S} = \begin{pmatrix} \mathbb{S}_{LS1}^K & 0 & 0 \\ 0 & \mathbb{S}_{LS1}^\nu & 0 \\ 0 & 0 & \mathbb{S}_{LS1}^Q \end{pmatrix}$$

So does the generalized Kirchhoff-compliance:

$$\mathbb{S}_{LS1}^K = \begin{pmatrix} \mathbb{S}_1^K & 0 & \dots & \dots & 0 \\ 0 & \mathbb{S}_2^K & 0 & \dots & \vdots \\ 0 & \ddots & \ddots & \ddots & \vdots \\ \vdots & \dots & \ddots & \ddots & 0 \\ 0 & \dots & \dots & 0 & \mathbb{S}_n^K \end{pmatrix} \quad (\text{A.11})$$

where  $\mathbb{S}_i^K$  refers to the Kirchhoff compliance of the  $i^{\text{th}}$  layer

$$\mathbb{S}_k^K = \begin{pmatrix} \frac{S_{11}^k}{e^k} & \frac{S_{12}^k}{e^k} & \frac{S_{16}^k}{e^k} & 0 & 0 & 0 \\ \frac{S_{21}^k}{e^k} & \frac{S_{22}^k}{e^k} & \frac{S_{26}^k}{e^k} & 0 & 0 & 0 \\ \frac{S_{16}^k}{e^k} & \frac{S_{26}^k}{e^k} & \frac{S_{66}^k}{e^k} & 0 & 0 & 0 \\ 0 & 0 & 0 & \frac{12S_{11}^k}{(e^k)^3} & \frac{12S_{12}^k}{(e^k)^3} & \frac{12S_{16}^k}{(e^k)^3} \\ 0 & 0 & 0 & \frac{12S_{12}^k}{(e^k)^3} & \frac{12S_{22}^k}{(e^k)^3} & \frac{12S_{26}^k}{(e^k)^3} \\ 0 & 0 & 0 & \frac{12S_{16}^k}{(e^k)^3} & \frac{12S_{26}^k}{(e^k)^3} & \frac{12S_{66}^k}{(e^k)^3} \end{pmatrix} \quad (\text{A.12})$$

in which  $S_{\alpha\beta} = S_{\alpha\alpha\beta\beta}$ ,  $S_{\alpha 6} = S_{\alpha\alpha 12}$  and  $S_{66} = S_{1212}$ .

The out-of-plane compliance admits the following tridiagonal structure:

$$\mathbb{S}^\nu = \begin{pmatrix} \frac{13(e^1 S_{3333}^1 + e^2 S_{3333}^2)}{35} & \frac{9e^2 S_{3333}^2}{70} & 0 & \dots & 0 \\ & \ddots & \ddots & \ddots & \vdots \\ & & \ddots & \ddots & 0 \\ & & & \ddots & \frac{9e^{n-1} S_{3333}^{n-1}}{70} \\ & & & & \frac{13(e^{n-1} S_{3333}^{n-1} + e^n S_{3333}^n)}{35} \end{pmatrix} \quad (\text{A.13})$$

Finally, the shear compliance collecting both intra and inter-laminar contributions reads:

$$\mathbb{S}^Q = \begin{pmatrix} \frac{6S_Q^1}{5e^1} & -\frac{S_Q^1}{10} & 0 & \cdot & \cdot & \cdot \\ -\frac{S_Q^1}{10} & \frac{2(\epsilon^1 S_Q^1 + e^2 S_Q^2)}{15} & -\frac{S_Q^2}{10} & -\frac{e^2 S_Q^2}{30} & 0 & \cdot \\ \cdot & 0 & -\frac{S_Q^2}{10} & \frac{6S_Q^2}{5e^2} & -\frac{S_Q^2}{10} & 0 \\ \cdot & 0 & -\frac{e^2 S_Q^2}{30} & -\frac{S_Q^2}{10} & \frac{2(\epsilon^2 S_Q^2 + e^3 S_Q^3)}{15} & -\frac{S_Q^3}{10} \\ \cdot & \cdot & \cdot & \cdot & \cdot & \cdot \\ \cdot & \cdot & \cdot & \cdot & \cdot & \frac{6S_Q^3}{5e^3} \end{pmatrix} \quad (\text{A.14})$$

where  $S_Q^k = [4S_{\alpha 3 \beta 3}^k]$

#### Appendix A.5. Lagrange condensation

$$\mathbf{T}^\top \cdot \boldsymbol{\Sigma} = 0 \quad \Rightarrow \quad \begin{cases} \mathbf{T}_m^{Q\top} \cdot \boldsymbol{\Sigma}^Q = 0 \\ \mathbf{T}_m^{\nu\top} \cdot \boldsymbol{\Sigma}^\nu = 0 \end{cases}$$

$\mathbf{T}_m^Q$  is a  $4n - 2 \times 2$ -matrix,  $\mathbf{T}_m^\nu$  is a  $n - 1$ -vector, with these notations (9) now reads:

$$\begin{aligned} \mathbb{C}_{corr}^\nu &= \mathbb{C}^\nu - \mathbb{C}^\nu \cdot \mathbf{T}_m^\nu \cdot \left( \mathbf{T}_m^{\nu\top} \cdot \mathbb{C}^\nu \cdot \mathbf{T}_m^\nu \right)^{-1} \mathbf{T}_m^{\nu\top} \cdot \mathbb{C}^\nu \\ \mathbb{C}_{corr}^Q &= \mathbb{C}^Q - \mathbb{C}^Q \cdot \mathbf{T}_m^Q \cdot \left( \mathbf{T}_m^{Q\top} \cdot \mathbb{C}^Q \cdot \mathbf{T}_m^Q \right)^{-1} \mathbf{T}_m^{Q\top} \cdot \mathbb{C}^Q \end{aligned} \quad (\text{A.15})$$

#### Appendix A.6. Critical stress identification

Following the discussion of section 5.3, the opening stress as a function of interfacial damage for a pure opening deformation mode with the density given in (57) reads:

$$\nu(d) = 2\sqrt{G_{Ic}c_\nu} \sqrt{\frac{\kappa_\nu(\kappa_\nu - 1)d(1-d)^{p+1}}{p(\kappa_\nu - d)^2}} \quad (\text{A.16})$$

One can then find the corresponding value of the damage parameter associated with the maximum stress, which is given by:

$$d_c = \frac{1 - \kappa_\nu}{\varsigma} + \varsigma + 1 \quad (\text{A.17})$$

$$\text{with } \varsigma = \sqrt[3]{(\sqrt{\kappa_\nu} - 1)(\kappa_\nu - 1)} \quad (\text{A.18})$$

for  $p = 1$ , and:

$$d_c = \frac{2\kappa_\nu - \sqrt{2\kappa_\nu(2\kappa_\nu - \frac{3}{2})}}{3} \quad (\text{A.19})$$

for  $p = 2$ .

Given some fixed interfacial material strength  $\sigma_c^\nu$ , the corresponding value for  $\kappa_\nu$  is found by solving the following scalar non-linear equation  $\nu(d_c) = \sigma_c^\nu$  in terms of  $\kappa_\nu$  for  $\nu(d_c)$  given by (A.16) and (A.17) or (A.19). Finally, a similar procedure is used to identify  $\kappa_\tau$  as function of a given interfacial shear strength  $\sigma_c^\tau$ .

In order to validate this procedure, Figures A.15-A.16 represent the computed opening stress as a function of an imposed interfacial opening  $\varepsilon_\nu$  for a laminate consisting of two plies and a single interface and various target interfacial strengths  $\sigma_c^\nu$ . The mechanical properties of the laminate are those of T300/977-2 carbon [68] with 0.192 mm thick plies.

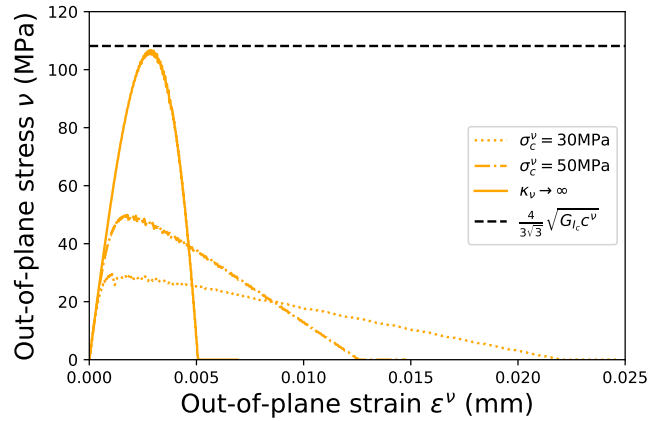


Figure A.15: Stress-deformation curve for a 2-ply laminate and various  $\sigma_c^\nu$   $p = 1$

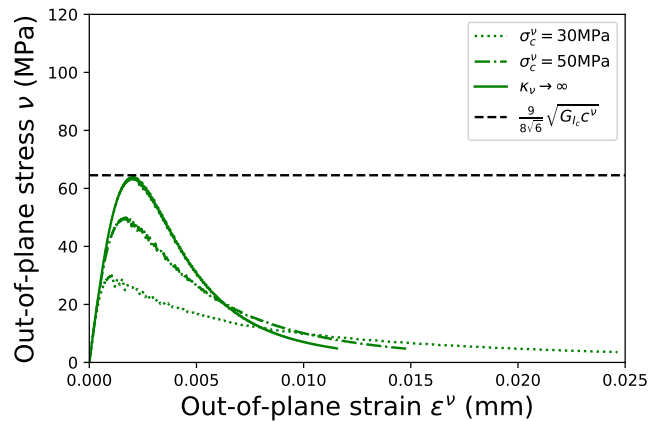


Figure A.16: Stress-deformation curve for a 2-ply laminate and various  $\sigma_c^\nu$   $p = 2$

## References

- [1] H. Zhang, E. Bilotti, T. Peijs, The use of carbon nanotubes for damage sensing and structural health monitoring in laminated composites: a review, *Nanocomposites 1* (2015) 167–184.
- [2] M. Marjanović, G. Meschke, D. Vuksanović, A finite element model for propagating delamination in laminated composite plates based on the virtual crack closure method, *Composite Structures 150* (2016) 8–19.
- [3] A. Köllner, Predicting buckling-driven delamination propagation in composite laminates: An analytical modelling approach, *Composite Structures 266* (2021) 113776.

- [4] A. Szekrényes, Application of differential quadrature method to delaminated first-order shear deformable composite plates, *Thin-Walled Structures* 166 (2021) 108028.
- [5] G. Alfano, M. Crisfield, Finite element interface models for the delamination analysis of laminated composites: mechanical and computational issues, *International Journal for Numerical Methods in Engineering* 50 (2001) 1701–1736.
- [6] G. Alfano, On the influence of the shape of the interface law on the application of cohesive-zone models, *Composites Science and Technology* 66 (2006) 723–730.
- [7] A. Turon, P. Camanho, J. Costa, J. Renart, Accurate simulation of delamination growth under mixed-mode loading using cohesive elements: definition of interlaminar strengths and elastic stiffness, *Composite structures* 92 (2010) 1857–1864.
- [8] J. Germain, J. Rannou, F. Laurin, Modélisation du délaminage: éléments d’interface et difficultés numériques, in: *Journées Nationales sur les Composites 2017*, 2017.
- [9] J. Reddy, A refined nonlinear theory of plates with transverse shear deformation, *International Journal of solids and structures* 20 (1984) 881–896.
- [10] J. Reddy, A generalization of two-dimensional theories of laminated composite plates, *Communications in applied numerical methods* 3 (1987) 173–180.
- [11] E. Carrera, Theories and finite elements for multilayered, anisotropic, composite plates and shells, *Archives of Computational Methods in Engineering* 9 (2002) 87–140.
- [12] E. Carrera, M. Cinefra, M. Petrolo, E. Zappino, *Finite element analysis of structures through unified formulation*, John Wiley & Sons, 2014.
- [13] I. Kaleel, E. Carrera, M. Petrolo, Progressive delamination of laminated composites via 1d models, *Composite Structures* 235 (2020) 111799.
- [14] M. Nagaraj, E. Carrera, M. Petrolo, Progressive damage analysis of composite laminates subjected to low-velocity impact using 2d layer-wise structural models, *International Journal of Non-Linear Mechanics* 127 (2020) 103591.
- [15] A. Eijo, E. Oñate, S. Oller, A numerical model of delamination in composite laminated beams using the lrz beam element based on the refined zigzag theory, *Composite Structures* 104 (2013) 270–280.
- [16] L. Škec, G. Jelenić, N. Lustig, Mixed-mode delamination in 2d layered beam finite elements, *International journal for numerical methods in engineering* 104 (2015) 767–788.
- [17] A. Köllner, C. Völlmecke, Post-buckling behaviour and delamination growth characteristics of delaminated composite plates, *Composite Structures* 203 (2018) 777–788.
- [18] N. Pagano, Stress fields in composite laminates, *International Journal of Solids and Structures* 14 (1978) 385–400.
- [19] A. Chabot, Analyse des efforts à l’interface entre les couches des matériaux composites à l’aide de modèles multiparticulaires de matériaux multicouches (M4), Ph.D. thesis, École Nationale des Ponts et Chaussées, 1997.
- [20] A. D. Diaz, J.-F. Caron, Interface plasticity and delamination onset prediction, *Mechanics of Materials* 38 (2006) 648–663.
- [21] T. Naciri, A. Ehrlacher, A. Chabot, Interlaminar stress analysis with a new multiparticle modelization of multilayered materials (m4), *Composites Science and Technology* 58 (1998) 337–343.
- [22] J.-F. Caron, A. D. Diaz, R. P. Carreira, A. Chabot, A. Ehrlacher, Multi-particle modelling for the prediction of delamination in multi-layered materials, *Composites Science and Technology* 66 (2006) 755–765.
- [23] A. D. Diaz, S. Chataigner, J.-F. Caron, et al., A layerwise finite element for multilayers with imperfect interfaces, *Composite Structures* 93 (2011) 3262–3271.
- [24] R. Baroud, K. Sab, J.-F. Caron, F. Kaddah, A statically compatible layerwise stress model for the analysis of multilayered plates, *International Journal of Solids and Structures* 96 (2016) 11–24.
- [25] L. Salha, J. Bleyer, K. Sab, J. Bodgi, Mesh-adapted stress analysis of multilayered plates using a layerwise model, *Advanced Modeling and Simulation in Engineering Sciences* 7 (2020) 2.
- [26] P. Bouteiller, J. Bleyer, K. Sab, Consistent derivation of stress-based generalized models in elastodynamics: application

- to layerwise plate models, *International Journal of Solids and Structures* (2021) 111077.
- [27] N. Saeedi, K. Sab, J.-F. Caron, Delaminated multilayered plates under uniaxial extension. part i: Analytical analysis using a layerwise stress approach, *International Journal of Solids and Structures* 49 (2012) 3711–3726.
- [28] N. Saeedi, K. Sab, J.-F. Caron, Delaminated multilayered plates under uniaxial extension. part ii: Efficient layerwise mesh strategy for the prediction of delamination onset, *International Journal of Solids and Structures* 49 (2012) 3727–3740.
- [29] A. Lerpiniere, J.-F. Caron, A. D. Diaz, K. Sab, The ls1 model for delamination propagation in multilayered materials at  $0^\circ/\theta^\circ$  interfaces: A comparison between experimental and finite elements strain energy release rates, *International Journal of Solids and Structures* 51 (2014) 3973–3986.
- [30] V. A. Duong, A. D. Diaz, S. Chataigner, J.-F. Caron, A layerwise finite element for multilayers with imperfect interfaces, *Composite Structures* 93 (2011) 3262–3271. URL: <https://www.sciencedirect.com/science/article/pii/S0263822311001607>. doi:<https://doi.org/10.1016/j.compstruct.2011.05.001>.
- [31] N. Saeedi, Une approche très efficace pour l’analyse du délaminage des plaques stratifiées infiniment longues, Ph.D. thesis, Paris Est, 2012.
- [32] V.-T. Nguyen, J.-F. Caron, A new finite element for free edge effect analysis in laminated composites, *Computers & structures* 84 (2006) 1538–1546.
- [33] N. Hongkarnjanakul, C. Bouvet, S. Rivallant, Validation of low velocity impact modelling on different stacking sequences of cfrp laminates and influence of fibre failure, *Composite Structures* 106 (2013) 549–559.
- [34] B. Halphen, Q. S. Nguyen, Sur les matériaux standard généralisés, *Journal de mécanique* 14 (1975) 39–63.
- [35] Q. S. Nguyen, *Stability and nonlinear solid mechanics*, Wiley, 2000.
- [36] E. M. Wu, R. Reuter Jr, Crack extension in fiberglass reinforced plastics, Technical Report, Illinois univ at urbana dept of theoretical and applied mechanics, 1965.
- [37] S. L. Donaldson, The effect of interlaminar fracture properties on the delamination buckling of composite laminates, *Composites Science and Technology* 28 (1987) 33–44.
- [38] S. Hashemi, A. Kinloch, J. Williams, Mechanics and mechanisms of delamination in a poly (ether sulphone)—fibre composite, *Composites Science and Technology* 37 (1990) 429–462.
- [39] B. Spencer, J. Barnby, The effects of notch and fibre angles on crack propagation in fibre-reinforced polymers, *Journal of Materials Science* 11 (1976) 83–88.
- [40] R. A. Jurf, R. B. Pipes, Interlaminar fracture of composite materials, *Journal of Composite Materials* 16 (1982) 386–394.
- [41] S. Donaldson, Fracture toughness testing of graphite/epoxy and graphite/peek composites, *Composites* 16 (1985) 103–112.
- [42] S. Mall, N. Kochhar, Criterion for mixed mode fracture in composite bonded joints, NASA report (1986).
- [43] M. L. Benzeggagh, M. Kenane, Measurement of mixed-mode delamination fracture toughness of unidirectional glass/epoxy composites with mixed-mode bending apparatus, *Composites Science and Technology* 56 (1996) 439–449.
- [44] A. C. Orifici, I. Herszberg, R. S. Thomson, Review of methodologies for composite material modelling incorporating failure, *Composite Structures* 86 (2008) 194–210.
- [45] M. Ortiz, L. Stainier, The variational formulation of viscoplastic constitutive updates, *Computer methods in applied mechanics and engineering* 171 (1999) 419–444.
- [46] C. Miehe, Strain-driven homogenization of inelastic microstructures and composites based on an incremental variational formulation, *International Journal for numerical methods in engineering* 55 (2002) 1285–1322.
- [47] A. Mielke, Evolution of rate-independent systems, *Evolutionary equations* 2 (2005) 461–559.
- [48] J.-Y. Wu, A unified phase-field theory for the mechanics of damage and quasi-brittle failure, *Journal of the Mechanics and Physics of Solids* 103 (2017) 72–99.
- [49] A. Logg, K.-A. Mardal, G. Wells, Automated solution of differential equations by the finite element method: The FEniCS book, volume 84, Springer Science & Business Media, 2012.

- [50] M. Alnæs, J. Blechta, J. Hake, A. Johansson, B. Kehlet, A. Logg, C. Richardson, J. Ring, M. E. Rognes, G. N. Wells, The fenics project version 1.5, *Archive of Numerical Software* 3 (2015).
- [51] J. Bleyer, *Numerical Tours of Computational Mechanics with FEniCS*, 2018. doi:10.5281/zenodo.1287832.
- [52] B. Bourdin, G. A. Francfort, J.-J. Marigo, Numerical experiments in revisited brittle fracture, *Journal of the Mechanics and Physics of Solids* 48 (2000) 797–826.
- [53] C. Miehe, M. Hofacker, F. Welschinger, A phase field model for rate-independent crack propagation: Robust algorithmic implementation based on operator splits, *Computer Methods in Applied Mechanics and Engineering* 199 (2010) 2765–2778.
- [54] M. Ambati, T. Gerasimov, L. De Lorenzis, A review on phase-field models of brittle fracture and a new fast hybrid formulation, *Computational Mechanics* 55 (2015) 383–405.
- [55] Y. Lu, T. Helfer, B. Bary, O. Fandeur, An efficient and robust staggered algorithm applied to the quasi-static description of brittle fracture by a phase-field approach, *Computer Methods in Applied Mechanics and Engineering* 370 (2020) 113218.
- [56] I. Ramière, T. Helfer, Iterative residual-based vector methods to accelerate fixed point iterations, *Computers & Mathematics with Applications* 70 (2015) 2210–2226.
- [57] E. Storvik, J. W. Both, J. M. Sargado, J. M. Nordbotten, F. A. Radu, An accelerated staggered scheme for variational phase-field models of brittle fracture, *Computer Methods in Applied Mechanics and Engineering* 381 (2021) 113822.
- [58] P. Farrell, C. Maurini, Linear and nonlinear solvers for variational phase-field models of brittle fracture, *International Journal for Numerical Methods in Engineering* 109 (2017) 648–667.
- [59] A. Corigliano, Formulation, identification and use of interface models in the numerical analysis of composite delamination, *International Journal of Solids and Structures* 30 (1993) 2779–2811.
- [60] L. Škec, G. Alfano, G. Jelenić, Complete analytical solutions for double cantilever beam specimens with bi-linear quasi-brittle and brittle interfaces, *International Journal of Fracture* 215 (2019) 1–37.
- [61] A. Szekrenyes, Improved analysis of unidirectional composite delamination specimens, *Mechanics of Materials* 39 (2007) 953–974.
- [62] M. Cabello, J. Zurbitu, J. Renart, A. Turon, F. Martínez, A general analytical model based on elastic foundation beam theory for adhesively bonded dcB joints either with flexible or rigid adhesives, *International Journal of Solids and Structures* 94 (2016) 21–34.
- [63] O. Allix, P. Ladeveze, A. Corigliano, Damage analysis of interlaminar fracture specimens, *Composite Structures* 31 (1995) 61–74.
- [64] J. Wang, P. Qiao, Novel beam analysis of end notched flexure specimen for mode-II fracture, *Engineering Fracture Mechanics* 71 (2004) 219–231.
- [65] A. K. Chen, M. Crisfield, Predicting progressive delamination of composite material specimens via interface elements, *Mechanics of Composite Materials and Structures* 6 (1999) 301–317.
- [66] P. Robinson, T. Besant, D. Hitchings, Delamination growth prediction using a finite element approach, in: *European Structural Integrity Society*, volume 27, Elsevier, 2000, pp. 135–147.
- [67] E. Iarve, D. Mollenhauer, Mesh-independent matrix cracking and delamination modeling in advanced composite materials, in: *Numerical modelling of failure in advanced composite materials*, Elsevier, 2015, pp. 227–264.
- [68] A. Morais, A. Marques, P. de Castro, Estudo da aplicação de ensaios de fractura interlaminar de modo I a laminados compostos multidireccionais, in: *Proceedings of the 7as jornadas de fractura*, Sociedade Portuguesa de Materiais, Portugal, 2000, pp. 90–95.